

AD-A173 519 CALCULATION OF VISCOUS TRANSONIC FLOWS ABOUT A
SUPERCritical AIRFOIL(U) UNIVERSAL ENERGY SYSTEMS INC
DAYTON OH M R VISBAL JUL 86 AFHAL-TR-86-3013

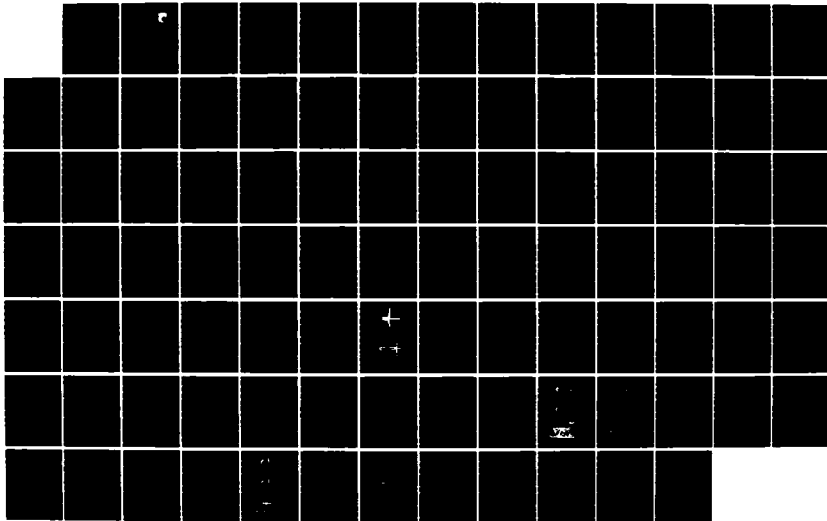
1/2

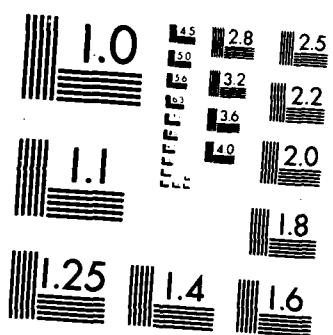
UNCLASSIFIED

F33615-83-C-3000

F/G 20/4

NL





MICROCOPY RESOLUTION TEST CHART
NATIONAL BUREAU OF STANDARDS 1963-A

AD-A173 519

AFWAL-TR-86-3013

CALCULATION OF VISCOUS TRANSONIC
FLOWS ABOUT A SUPERCRITICAL AIRFOIL



Miguel R. Visbal
Universal Energy Systems, Inc.
4401 Dayton-Xenia Road
Dayton, OH 45432

July 1986

Final Report for Period August 1983 - November 1984

Approved for public release; distribution unlimited.

AMIC FILE COPY

FLIGHT DYNAMICS LABORATORY
AIR FORCE WRIGHT AERONAUTICAL LABORATORIES
AIR FORCE SYSTEMS COMMAND
WRIGHT-PATTERSON AIR FORCE BASE, OHIO 45433-6553

CC 5 2 1986

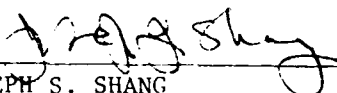
86 10 30 010

NOTICE

When Government drawings, specifications, or other data are used for any purpose other than in connection with a definitely related Government procurement operation, the United States Government thereby incurs no responsibility nor any obligation whatsoever; and the fact that the government may have formulated, furnished, or in any way supplied the said drawings, specifications, or other data, is not to be regarded by implication or otherwise as in any manner licensing the holder or any other person or corporation, or conveying any rights or permission to manufacture use, or sell any patented invention that may in any way be related thereto.

This report has been reviewed by the Office of Public Affairs (ASD/PA) and is releasable to the National Technical Information Service (NTIS). At NTIS, it will be available to the general public, including foreign nations.

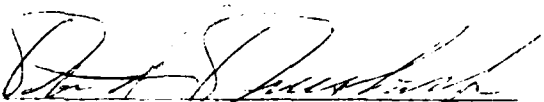
This technical report has been reviewed and is approved for publication.



JOSEPH S. SHANG
Technical Manager



TOMMY J. KENT, Maj, USAF
Chief, Aerodynamics & Airframe Branch
Aeromechanics Division



DONALD A. DREESBACH, Col, USAF
Chief, Aeromechanics Division

"If your address has changed, if you wish to be removed from our mailing list, or if the addressee is no longer employed by your organization please notify AFWAL/FIMM, W-PAFB, OH 45433 to help us maintain a current mailing list".

Copies of this report should not be returned unless return is required by security considerations, contractual obligations, or notice on a specific document.

UNCLASSIFIED

ACA 193519

SECURITY CLASSIFICATION OF THIS PAGE

REPORT DOCUMENTATION PAGE

1a. REPORT SECURITY CLASSIFICATION Unclassified		1b. RESTRICTIVE MARKINGS										
2a. SECURITY CLASSIFICATION AUTHORITY		3. DISTRIBUTION/AVAILABILITY OF REPORT Approved for public release; distribution unlimited										
2b. DECLASSIFICATION/DOWNGRADING SCHEDULE												
4. PERFORMING ORGANIZATION REPORT NUMBER(S)		5. MONITORING ORGANIZATION REPORT NUMBER(S) AFWAL-TR-86-3013										
6a. NAME OF PERFORMING ORGANIZATION Universal Energy Systems, Inc.	6b. OFFICE SYMBOL (If applicable)	7a. NAME OF MONITORING ORGANIZATION Air Force Wright Aeronautical Laboratories Flight Dynamics Laboratory (AFWAL/FIMM)										
6c. ADDRESS (City, State and ZIP Code) 4401 Dayton-Xenia Road Dayton, OH 45432		7b. ADDRESS (City, State and ZIP Code) Wright-Patterson AFB, OH 45433-6553										
8a. NAME OF FUNDING/SPONSORING ORGANIZATION Flight Dynamics Laboratory	8b. OFFICE SYMBOL (If applicable) AFWAL/FIMM	9. PROCUREMENT INSTRUMENT IDENTIFICATION NUMBER F33615-83-C-3000										
8c. ADDRESS (City, State and ZIP Code) Wright-Patterson AFB, OH 45433-6553		10. SOURCE OF FUNDING NOS. <table border="1"> <tr> <td>PROGRAM ELEMENT NO. 61102F</td> <td>PROJECT NO. 2307</td> <td>TASK NO. N6</td> <td>WORK UNIT NO. 11</td> </tr> </table>		PROGRAM ELEMENT NO. 61102F	PROJECT NO. 2307	TASK NO. N6	WORK UNIT NO. 11					
PROGRAM ELEMENT NO. 61102F	PROJECT NO. 2307	TASK NO. N6	WORK UNIT NO. 11									
11. TITLE (Include Security Classification) Calculation of Viscous Transonic Flows About a Supercritical Airfoil												
12. PERSONAL AUTHOR(S) Miguel R. Visbal												
13a. TYPE OF REPORT Final	13b. TIME COVERED FROM Aug 83 TO Nov 84	14. DATE OF REPORT (Yr., Mo., Day) July 1986	15. PAGE COUNT 91									
16. SUPPLEMENTARY NOTATION (cont'd. on back)												
17. COSATI CODES <table border="1"> <tr> <th>FIELD</th> <th>GROUP</th> <th>SUB. GR.</th> </tr> <tr> <td>01</td> <td>01</td> <td></td> </tr> <tr> <td>20</td> <td>04</td> <td></td> </tr> </table>		FIELD	GROUP	SUB. GR.	01	01		20	04		18. SUBJECT TERMS (Continue on reverse if necessary and identify by block number) Navier-Stokes Equations, Computational Fluid Dynamics, Airfoils, MacCormack's Explicit Algorithm, Beam-Warming Algorithm, Transonic Flow, Numerical methods, (over)	
FIELD	GROUP	SUB. GR.										
01	01											
20	04											
19. ABSTRACT (Continue on reverse if necessary and identify by block number) A critical examination of several aspects of the numerical simulation of high Reynolds number transonic airfoil flows is presented. Subcritical and supercritical flow fields about an aft-cambered airfoil were generated by solving the mass-averaged Navier-Stokes equations with turbulence incorporated through an algebraic eddy viscosity model. The governing equations were solved on curvilinear body-fitted grids utilizing two different algorithms, i.e. MacCormack's explicit and Beam-Warming implicit. The numerical uncertainties associated with different schemes, grid resolution, artificial viscosity and far field boundary placement were investigated and found to be of the same order of magnitude or less than the corresponding uncertainties in the available experimental data. Comparison of computed and experimental results showed good prediction of all the essential flow features. However, detailed comparison of velocity profiles pointed out deficiencies of the turbulence model downstream of the shock/boundary layer interaction in the airfoil cove and in the near-wake. Thin-layer and Navier-Stokes computed results (over)												
20. DISTRIBUTION/AVAILABILITY OF ABSTRACT UNCLASSIFIED/UNLIMITED <input checked="" type="checkbox"/> SAME AS RPT <input type="checkbox"/> DTIC USERS <input type="checkbox"/>		21. ABSTRACT SECURITY CLASSIFICATION Unclassified										
22a. NAME OF RESPONSIBLE INDIVIDUAL Joseph S. Shang		22b. TELEPHONE NUMBER (Include Area Code) (513) 255-2455	22c. OFFICE SYMBOL AFWAL/FIMM									

UNCLASSIFIED

SECURITY CLASSIFICATION OF THIS PAGE

were found in excellent agreement with each other. However, the Euler equations failed to provide a reasonable approximation of the flow due to the dramatic viscous-inviscid interaction effects for supercritical airfoils. *Keywords:*

UNCLASSIFIED

SECURITY CLASSIFICATION OF THIS PAGE

FOREWORD

This report is the result of research performed in the Computational Aerodynamics Group, Aerodynamics and Airframe Branch, Aeromechanics Division, Flight Dynamics Laboratory from August 1983 to November 1984. This report was prepared by Dr. Miguel R. Visbal, Visiting Scientist, under work unit 2307N603, "Computational Fluid Dynamics," with Dr. Wylbur Hankey as the Task Manager. The report was submitted in March 1985.

The author would like to express his appreciation to Dr. Wylbur Hankey and Dr. Joseph Shang for their valuable technical guidance and advice during this work. My association with all the members of the Computational Aerodynamics Group has been both personally and technically rewarding.

Computer time for the present study was provided in part by the NASA Ames Research Center.



A-1

TABLE OF CONTENTS

<u>SECTION</u>		<u>PAGE</u>
I	INTRODUCTION	1
II	MATHEMATICAL DESCRIPTION OF THE FLOW	5
	1. Governing Equations	5
	2. Boundary and Initial Conditions	10
	3. Turbulence Model	12
III	NUMERICAL PROCEDURE	15
	1. Generation of Computational Grids	15
	a. Intermediate Transformation	15
	b. Final Transformation	17
	2. Implicit Navier-Stokes Code	19
	3. Explicit Navier-Stokes Code	21
	4. Steady-State Convergence Criterion	23
	5. Calculation of Airfoil Force Coefficients	24
IV	RESULTS AND DISCUSSION	27
	1. Flow Configuration and Computational Details . . .	27
	2. Results for Subcritical Case	31
	3. Results for Supercritical Case	35
	4. Investigation of Numerical Error due to Damping .	38

TABLE OF CONTENTS (continued)

<u>SECTION</u>		<u>PAGE</u>
V	CONCLUSIONS AND RECOMMENDATIONS	41
APPENDIX A	CONSTANTS FOR FAR-WAKE TURBULENCE MODEL . .	43
APPENDIX B	JACOBIAN MATRICES FOR THE NAVIER-STOKES EQUATIONS	45
REFERENCES	79

LIST OF ILLUSTRATIONS

FIGURE		PAGE
1	Basic Transformation	47
2	Regions for Turbulence Model	48
3	Boundary - Fitted Grid	49
4	Convergence of C_L and C_D for Implicit Code (Airfoil Subcritical Case, Coarse grid)	50
5	Convergence of Skin Friction Coefficient for Explicit Code (Supersonic Flat Plate Boundary Layer with Blowing)	51
6	Convergence of C_L and C_D for Explicit Code (Airfoil Subcritical Case, Fine Grid)	52
7	Variation of Computed C_p and C_L with Angle of Attack, Subcritical Case	53
8	Effect of Variation of Near-Wake Relaxation Length (Equation (2.31)), Subcritical Case	54
9	Effect of Damping Coefficient on Subcritical Case, Coarse Grid	55
10	Effect of Grid Resolution on Computed Subcritical Flow, Implicit Code	56
11	Computed Mach Number Contours for Subcritical Case, Implicit Code	57
12	Effect of Grid Resolution on Computed Subcritical Flow, Explicit Code	58
13	Computed Mach Number Contours for Subcritical Case, Explicit Code	59
14	Computed and Experimental C_p , C_L and C_D for subcritical Case, Coarse Grid	60
15	Computed and Experimental C_p , C_L and C_D for Subcritical Case, Medium Grid	61
16	Computed and Experimental C_p , C_L and C_D for Subcritical Case, Fine Grid	62

LIST OF ILLUSTRATIONS (Continued)

FIGURE		PAGE
17	Computed and Experimental Velocity Profiles for Subcritical Case, Upper Surface	63
18	Computed and Experimental Velocity Profiles for Subcritical Case, Lower Surface	64
19	Computed and Experimental Velocity Profiles for Subcritical Case, Near-Wake	65
20	Comparison of Computed Density Contours and Experimental Interferogram, Subcritical Case	66
21	Detailed Comparison of Computed Density Contours and Experimental Interferogram near Airfoil Trailing Edge, Subcritical Case	67
22	Repeatability of Experimental Static-Pressure Measurements (Reference 4)	68
23	Effect of Freestream Mach Number on Shock Location for Supercritical Case, Explicit Code	69
24	Effect of Farfield Boundary Placement on Computed Supercritical flow, Explicit Code	70
25	Computed and Experimental C_p , C_L and C_D for Supercritical Case	71
26	Computed and Experimental Velocity Profiles for Supercritical Case, Upper Surface	72
27	Computed and Experimental Velocity Profiles for Supercritical Case, Lower Surface	73
28	Computed and Experimental Velocity Profiles for Supercritical Case, Near-Wake	74
29	Comparison of Computed Density Contours and Experimental Interferogram, Supercritical Case	75
30	Comparison of Euler, Thin-Layer and Navier-Stokes Results for Supercritical Case, Implicit Code	76

LIST OF ILLUSTRATIONS (Continued)

FIGURE		PAGE
31	Contours of Damping-to-Truncation Error Ratio for Density Equation, Supercritical Case	77
32	Contours of Artificial-to-True Viscosity Ratio in Streamwise Momentum Equation, Explicit Code (Fine Grid)	78

LIST OF TABLES

TABLE		PAGE
1	Flow Parameters	29
2	Grid Details	29
3	Comparison of Computer Times for Explicit and Implicit Codes	30
4	Damping-to-Truncation Error Ratio for the Continuity Equation	40

LIST OF SYMBOLS

A	Jacobian matrix for implicit algorithm, Equation (3.13)
a	Speed of sound,
B	Jacobian matrix for implicit algorithm, Equation (3.13)
b_i	Viscous coefficients, Equation (2.17)
CFL	Courant number
C_{cp}	Constant in outer turbulent eddy viscosity formulation
C_D	Section drag coefficient
C_{kleb}	Constant in Klebanoff intermittency factor
C_L	Section lift coefficient
C_p	Pressure coefficient, $2(p-p_\infty)/\rho_\infty U_\infty^2$
C_p^*	Critical pressure coefficient ($M = 1$)
C_{wk}	Constant in far-wake turbulence model
c	Airfoil chord
c_i	Viscous coefficients, Equation (2.18)
c_p	Specific heat at constant pressure
D	Van Driest damping factor, Equation (2.25)
d_i	Viscous coefficients, Equation (2.19)
e	Total energy per unit mass
F, \hat{F}	Flux vectors, Equations (2.3) and (2.9)
F_{kleb}	Klebanoff intermittency factor, Equation (2.28)
F_{max}	Velocity scale in turbulence model
G, \hat{G}	Flux vectors, Equations (2.3) and (2.9)
IL	No. of grid points in ξ - direction
J	Transformation Jacobian
K	von Karman's constant

LIST OF SYMBOLS (Continued)

k	Clauser's constant
M	Jacobian matrix for implicit algorithm, Equation (3.13)
M_∞	Freesream Mach Number
N	Jacobian matrix for implicit algorithm, Equation (3.13)
P	Grid control function, Equation (3.5)
Pr	Molecular Prandtl number
Pr_t	Turbulent Prandtl number
p	Static pressure
Q	Grid control function, Equation (3.6)
q, \hat{q}	Vectors of dependent variables, Equations (2.2) and (2.9)
R	Grid control function, Equation (3.8); gas constant
Re_c	Chord Reynolds number, $\rho_\infty U_\infty c / \mu_\infty$
S	Grid control function, Equation (3.7)
T	Absolute temperature; grid control function, Equation (3.9)
t	Time
u, v	Contravariant velocity components
U	Velocity, $(u^2 + v^2)^{1/2}$
u, v	Cartesian velocity components
x, y	Cartesian coordinates parallel and normal to airfoil chord respectively
Y	Distance normal to airfoil surface for boundary layer turbulence model; distance measured from wake centerline
Y_{max}	Length scale in turbulence model
GREEK SYMBOLS:	
α	Angle of attack

LIST OF SYMBOLS (Concluded)

β	Damping coefficient in explicit algorithm, Equation (3.21)
γ	Specific heat ratio
$\Delta s_\xi, \Delta s_\eta$	Grid spacing in physical plane, Equations (3.24) and (3.25)
Δt	Time step
δ_ξ, δ_η	Finite-difference operators, Equation (3.17)
$\varepsilon_i, \varepsilon_o$	Turbulent eddy viscosity in boundary layer inner and outer regions respectively
$\varepsilon_{nk}, \varepsilon_{wk}$	Turbulent eddy viscosity in near-wake and far-wake respectively
ϕ	Grid control function, Equation (3.1)
λ_T	Second coefficient of viscosity, $\lambda_T = -2/3 (\mu + \varepsilon)$
μ	Molecular dynamic viscosity
μ_ξ, μ_η	Finite-difference operators, equation (3.17)
ξ, η	Transformed coordinates
ρ	Density
$\tau_{xx}, \tau_{xy}, \tau_{yy}$	Viscous stress components, Equation (2.4)
ω	Vorticity
ω_e, ω_i	Damping coefficients in implicit algorithm, Equations (3.18) and (3.19)
SUBSCRIPTS	
i, j	Mesh indices
w	Wall conditions
∞	Freestream conditions

SECTION I INTRODUCTION

In recent years, the numerical simulation of high Reynolds number transonic flows over airfoils has been presented in numerous publications. A comprehensive review of the subject can be found, for example, in References 1 and 2, and therefore is not repeated here. This earlier work clearly illustrates the potential of Navier-Stokes numerical methods for evolving into a reliable predictive design technique. However, for this goal to be attained, two major problem areas still require further investigation. First, an assessment of the accuracy of the computed solutions must be conducted in order to clarify the uncertainties due to grid resolution, boundary condition formulation and numerical damping. Second, a suitable turbulence model must be developed, capable of accurately describing flows containing transition, separation, wakes and shock wave/boundary layer interactions. This second problem area clearly constitutes the pacing item in computational aerodynamics and will most likely require a continued process of numerical evaluation of different turbulence modeling formulations. For this evaluation process to be meaningful, the degree of uncertainty associated with the numerical simulations must be first established. It should be noted, however, that numerical resolution and turbulence modeling cannot be entirely separated since grid resolution is dependent on the turbulence model employed.

Since "exact" solutions are not generally available for complex transonic flows of interest, grid refinement studies constitute the only suitable alternative for accuracy assessment. Even for two-dimensional flows, this approach can be very costly in terms of computer resources and therefore the accuracy of the numerical solutions is customarily judged by comparison with available experimental data. However, comparing computed and experimental results can be inconclusive due to (1) lack of numerical resolution, (2) uncertainties in the measurements (e.g. wind tunnel and probe interference), and (3) the inability to isolate numerical errors from those due to turbulence modeling. With the advent of powerful computers, more detailed calculations of two-dimensional transonic viscous flows are now possible³, and should help clarify some of the uncertainties inherent to the numerical simulations.

With the above background as motivation, the present research critically examines several aspects of the numerical solution of the Navier-Stokes equations for high Reynolds number transonic airfoil flows. This problem embodies many interesting flow features such as leading and trailing edge regions, wake and shock/boundary layer interactions. The particular configuration considered was a modified Whitcomb supercritical airfoil, denoted as DSMA 523.⁴ This airfoil exhibits significant rear-loading and a strong viscous-inviscid interaction as compared with more conventional sections having little or no aft-camber. In addition, this airfoil was selected as one of the test cases for the 1980 Stanford conference on complex turbulent flows.⁵

Computations were performed using the mass-averaged Navier-Stokes equations⁶ expressed in terms of general curvilinear coordinates and with turbulence represented by an algebraic eddy viscosity model.⁷ The governing equations were solved in nearly-orthogonal body-fitted grids⁸ employing MacCormack's explicit scheme⁹ and the implicit Beam-Warming algorithm.¹⁰ These two most commonly used numerical schemes were chosen for their intrinsic differences in solving the system of governing equations. A direct comparison between the two algorithms was performed under identical mesh systems, boundary conditions and turbulence model. Such a one-to-one comparison, the author believes, has not been previously documented in the literature.

The main objectives in this investigation of transonic airfoil flows can be summarized as follows:

- (1) A comparative study of the relative accuracy between an explicit and an implicit Navier-Stokes code.
- (2) Effects of grid refinement, numerical damping and farfield boundary placement on the computed flowfields.
- (3) Comparison of the results obtained with the Euler, the thin-layer and the full Navier-Stokes equations.
- (4) Evaluation of the algebraic turbulent eddy viscosity model by detailed comparison of computed and experimental data for both subcritical and supercritical flows.

SECTION II

MATHEMATICAL DESCRIPTION OF THE FLOW

In this investigation, viscous transonic airfoil flows are simulated by means of the two-dimensional compressible Navier-Stokes equations. The governing equations are written in terms of general curvilinear coordinates and mass-averaged variables, with turbulence incorporated through an algebraic eddy viscosity model. The particular form of the flow equations, turbulence model and boundary conditions employed are presented in this section.

1. GOVERNING EQUATIONS

The governing equations are taken to be the two-dimensional compressible Navier-Stokes equations expressed in terms of mass-averaged variables⁶ and general curvilinear coordinates with turbulence represented by an algebraic eddy viscosity model. Two different forms of the equations are employed in this research. The explicit numerical algorithm (described in Section III) utilizes the chain-rule conservative form¹¹, while the implicit scheme solves the strong conservative formulation.¹²

In terms of general curvilinear coordinates (ξ, η), the chain-rule conservative Navier-Stokes equations can be written as follows:

$$\frac{\partial \mathbf{q}}{\partial t} + \xi_x \frac{\partial \mathbf{F}}{\partial \xi} + \xi_y \frac{\partial \mathbf{G}}{\partial \xi} + \eta_x \frac{\partial \mathbf{F}}{\partial \eta} + \eta_y \frac{\partial \mathbf{G}}{\partial \eta} = 0 \quad (2.1)$$

where

$$\mathbf{q} = [\rho, \rho u, \rho v, \rho e]^T \quad (2.2)$$

$$F = \begin{pmatrix} \rho u \\ \rho u^2 + p - \tau_{xx} \\ \rho u v - \tau_{xy} \\ (\rho e + p)u - F_4 \end{pmatrix}; \quad G = \begin{pmatrix} \rho v \\ \rho u v - \tau_{xy} \\ \rho v^2 + p - \tau_{yy} \\ (\rho e + p)v - G_4 \end{pmatrix} \quad (2.3)$$

and

$$\begin{aligned} \tau_{xx} &= 2(\mu + \varepsilon)u_x + \lambda_T(u_x + v_y) \\ \tau_{xy} &= (\mu + \varepsilon)(u_y + v_x) \\ \tau_{yy} &= 2(\mu + \varepsilon)v_y + \lambda_T(u_x + v_y) \\ F_4 &= u\tau_{xx} + v\tau_{xy} + c_p\left(\frac{\mu}{Pr} + \frac{\varepsilon}{Pr}\right)T_x \\ G_4 &= u\tau_{xy} + v\tau_{yy} + c_p\left(\frac{\mu}{Pr} + \frac{\varepsilon}{Pr}\right)T_y \end{aligned} \quad (2.4)$$

The variables u and v denote respectively the x and y velocity components. The density ρ , static pressure p and the absolute temperature T satisfy the equation of state for a perfect gas

$$p = \rho RT = (\gamma - 1) [\rho e - \frac{1}{2} \rho (u^2 + v^2)] \quad (2.5)$$

where e is the total energy per unit mass, R is the gas constant ($1716 \text{ ft}^2/\text{sec}^2 \cdot {}^\circ\text{R}$ for air) and γ ($= 1.4$) is the ratio of specific heats. The dynamic molecular viscosity μ is obtained from Sutherland's formula. The turbulent eddy viscosity ε is given by the eddy viscosity model which will be discussed later. Stokes hypothesis is assumed (i.e., $\lambda_T = -2/3(\mu + \varepsilon)$). The molecular Prandtl number Pr , the turbulent Prandtl number

\Pr_t and the specific heat c_p are taken to be constant ($\Pr = 0.72$,

$\Pr_t = 0.9$ and $c_p = 6006 \text{ ft}^2/\text{sec}^2 - {}^\circ\text{R}$)

The quantities ξ_x , ξ_y , η_x , η_y denote the transformation metrics (see Figure 1 for an sketch of the basic transformation)

$$\begin{aligned}\xi_x &= y \eta & \xi_y &= -x \eta \\ \eta_x &= -y \xi & \eta_y &= x \xi\end{aligned}\quad (2.6)$$

where J is the transformation Jacobian

$$J = \frac{\partial(\xi, \eta)}{\partial(x, y)} = \xi_x \eta_y - \xi_y \eta_x = 1/(\xi_x y \eta - \xi_y x \eta) \quad (2.7)$$

The Navier-Stokes equations (2.1) can be cast in strong conservation form¹² as follows

$$\frac{\partial \hat{q}}{\partial t} + \frac{\partial \hat{F}}{\partial \xi} + \frac{\partial \hat{G}}{\partial \eta} = 0 \quad (2.8)$$

where

$$\begin{aligned}\hat{q} &= q/J \\ \hat{F} &= (\xi_x F + \xi_y G)/J \\ \hat{G} &= (\eta_x F + \eta_y G)/J\end{aligned}\quad (2.9)$$

In order to facilitate the implementation of the implicit algorithm (Section III), Equation (2.8) is rewritten in the following fashion

$$\begin{aligned}\frac{\partial \hat{q}}{\partial t} + \frac{\partial E_1}{\partial \xi} + \frac{\partial E_2}{\partial \eta} &= \frac{\partial V_1}{\partial \xi} (\hat{q}, \hat{q}_\xi) + \frac{\partial V_2}{\partial \xi} (\hat{q}, \hat{q}_\eta) \\ &+ \frac{\partial W_1}{\partial \eta} (\hat{q}, \hat{q}_\xi) + \frac{\partial W_2}{\partial \eta} (\hat{q}, \hat{q}_\eta)\end{aligned}\quad (2.10)$$

where

$$E_1 = \frac{1}{J} \begin{pmatrix} \rho ll \\ \rho uu + \xi_x p \\ \rho vu + \xi_y p \\ (\rho + \rho e)u \end{pmatrix} \quad E_2 = \frac{1}{J} \begin{pmatrix} \rho V \\ \rho uV + \eta_x p \\ \rho vV + \eta_y p \\ (\rho + \rho e) V \end{pmatrix} \quad (2.11)$$

$$V_1 = \frac{1}{J} \begin{pmatrix} 0 \\ b_1 u_\xi + b_2 v_\xi \\ b_2 u_\xi + b_3 v_\xi \\ b_1 uu_\xi + b_2 (vu_\xi + uv_\xi) + b_3 vv_\xi + b_4 T_\xi \end{pmatrix} \quad (2.12)$$

$$V_2 = \frac{1}{J} \begin{pmatrix} 0 \\ c_1 u_\eta + c_2 v_\eta \\ c_3 u_\eta + c_4 v_\eta \\ c_1 uu_\eta + c_2 uv_\eta + c_3 vu_\eta + c_4 vv_\eta + c_5 T_\eta \end{pmatrix} \quad (2.13)$$

$$W_1 = \frac{1}{J} \begin{pmatrix} 0 \\ c_1 u_\xi + c_3 v_\xi \\ c_2 u_\xi + c_4 v_\xi \\ c_1 uu_\xi + c_2 vu_\xi + c_3 uv_\xi + c_4 vv_\xi + c_5 T_\xi \end{pmatrix} \quad (2.14)$$

$$W_2 = \frac{1}{J} \begin{pmatrix} 0 \\ d_1 u_\eta + d_2 v_\eta \\ d_2 u_\eta + d_3 v_\eta \\ d_1 uu_\eta + d_2 (vu_\eta + uv_\eta) + d_3 vv_\eta + d_4 T_\eta \end{pmatrix} \quad (2.15)$$

u, v denote the contravariant velocities

$$\begin{aligned} u &= \xi_x u + \xi_y v \\ v &= \eta_x u + \eta_y v \end{aligned} \quad (2.16)$$

and the viscous coefficients b_i, c_i, d_i are

$$\begin{aligned} b_1 &= (\mu + \epsilon) \left(\frac{4}{3} \xi_x^2 + \xi_y^2 \right) \\ b_2 &= \frac{1}{3} (\mu + \epsilon) \xi_x \xi_y \\ b_3 &= (\mu + \epsilon) \left(\xi_x^2 + \frac{4}{3} \xi_y^2 \right) \\ b_4 &= c_p \left(\frac{\mu}{p_r} + \frac{\epsilon}{p_{r_t}} \right) \left(\xi_x^2 + \xi_y^2 \right) \end{aligned} \quad (2.17)$$

$$\begin{aligned} c_1 &= -(\mu + \epsilon) \left(\frac{4}{3} \xi_x \eta_x + \xi_y \eta_y \right) \\ c_2 &= -(\mu + \epsilon) \left(\frac{2}{3} \xi_x \eta_y - \xi_y \eta_x \right) \\ c_3 &= (\mu + \epsilon) \left(\xi_x \eta_y - \frac{2}{3} \xi_y \eta_x \right) \\ c_4 &= -(\mu + \epsilon) \left(\xi_x \eta_x + \frac{4}{3} \xi_y \eta_y \right) \\ c_5 &= -c_p \left(\frac{\mu}{p_r} + \frac{\epsilon}{p_{r_t}} \right) \left(\xi_x \eta_x + \xi_y \eta_y \right) \end{aligned} \quad (2.18)$$

$$\begin{aligned} d_1 &= (\mu + \epsilon) \left(\frac{4}{3} \eta_x^2 + \eta_y^2 \right) \\ d_2 &= \frac{1}{3} (\mu + \epsilon) \eta_x \eta_y \\ d_3 &= (\mu + \epsilon) \left(\eta_x^2 + \frac{4}{3} \eta_y^2 \right) \\ d_4 &= c_p \left(\frac{\mu}{p_r} + \frac{\epsilon}{p_{r_t}} \right) \left(\eta_x^2 + \eta_y^2 \right) \end{aligned} \quad (2.19)$$

By neglecting the viscous terms in the direction parallel to a solid surface, the so called thin-layer approximation⁷ is obtained. Assuming a body-conforming curvilinear coordinate system, with the ξ and η directions defined as shown in Figure 1, the thin-layer Navier-Stokes equations become

$$\frac{\partial \hat{q}}{\partial t} + \frac{\partial E_1}{\partial \xi} + \frac{\partial E_2}{\partial \eta} = \frac{\partial W_2}{\partial \eta} (\hat{q}, \hat{q}_m) \quad (2.20)$$

Finally, the Euler equations are obtained by neglecting all viscous terms (i.e., by setting the right-hand-side of Equation (2.20) equal to zero).

2. BOUNDARY AND INITIAL CONDITIONS

In order to completely define the problem, suitable boundary and initial conditions must be specified. Referring to the airfoil computational domain shown in Figure 1, the following boundary conditions are prescribed.

Along the outer boundary ABC, freestream conditions are given for all the flow variables. On the downstream boundaries AD and HC,

$$\begin{aligned} P &= P_{\infty} \\ \frac{\partial}{\partial \xi} \begin{pmatrix} P \\ u \\ v \end{pmatrix} &= 0 \end{aligned} \quad (2.21)$$

Since the above farfield conditions are only approximate, the effect of the placement of the downstream and outer boundaries will be considered in Section IV.

Along the airfoil surface, the no-slip adiabatic conditions

$$\begin{aligned} u &= v = 0 \\ \frac{\partial}{\partial \eta} \left(\frac{p}{T} \right) &= 0 \end{aligned} \quad (2.22)$$

are imposed for viscous flows. For the Euler equations, the conditions

$$\begin{aligned} v &= 0 \\ \frac{\partial}{\partial \eta} \left(\frac{u}{\rho} \right) &= 0 \\ (n_x^2 + n_y^2) p_n &= -\rho u (n_x u_\xi + n_y v_\xi) \end{aligned} \quad (2.23)$$

are specified, where u , v are the contravariant velocities, Equation (2.16). The boundary conditions (2.22) and (2.23) are applied in conjunction with a body-fitted grid which is nearly orthogonal at the airfoil surface.

Finally, along the wake-cut ED, averaging is used for all the flow variables so as to ensure continuity.

Since only steady flows are considered in this research, initial conditions are not of primary concern to provide a converged numerical solution. A simple uniform flow initial condition was always employed in the present airfoil calculations, unless previous computed results were already available.

3. TURBULENCE MODEL

Turbulence is simulated by a modified version of the algebraic eddy viscosity model of Baldwin and Lomax⁷. As depicted in Figure 2, three separate regions are considered in the implementation of the turbulence model. Namely, the airfoil boundary layers, the near-wake in the vicinity of the airfoil trailing edge and the far-wake.

In the airfoil boundary layers, a two-layer formulation is employed. The inner turbulent eddy viscosity ϵ_i is given by the Prandtl - Van Driest expression

$$\epsilon_i = \rho (kYD)^2 |\omega| \quad (2.24)$$

$$D = 1 - \exp \left[- \gamma \left(\frac{\rho_w |\omega_w|}{\mu_w} \right)^{1/2} / 26 \right] \quad (2.25)$$

$$|\omega| = \left| \frac{\partial u}{\partial y} - \frac{\partial v}{\partial x} \right| \quad (2.26)$$

where ω is the vorticity, Y represents the distance normal to the airfoil surface, $K = 0.40$ is von Karman's constant and the subscript w denotes values at the wall.

In the outer region of the boundary layer, the turbulent eddy viscosity ϵ_o is defined as follows

$$\epsilon_o = \rho k C_{cp} Y_{max} F_{max} F_{kleb} \quad (2.27)$$

where $F_{\max} = \max (Y|\omega|D)$, Y_{\max} is the value of Y at which F_{\max} occurs,

$$F_{\text{kleb}} = \left[1 + 5.5 \left(C_{\text{kleb}} \frac{Y_{\max}}{Y} \right)^6 \right]^{-1} \quad (2.28)$$

and

$$k = 0.0168, \quad C_{cp} = 1.6, \quad C_{\text{kleb}} = 0.3$$

The turbulence model switches from the inner to the outer formulation at the first value of Y away from the wall where $\epsilon_i \geq \epsilon_0$. Transition is simulated by simply beginning the application of the above turbulence model at the boundary layer trip locations specified in the experiments.⁴

The far-wake turbulent eddy viscosity ϵ_{wk} is computed as follows

$$\epsilon_{wk} = \rho C_{wk} \frac{Y_{\max} U^2 DIF}{F_{\max}} F_{\text{kleb}} \quad (2.29)$$

where

$$\begin{aligned} F_{\max} &= \max (Y|\omega|) \\ U_{\text{DIF}} &= (u^2 + v^2)_{\max}^{1/2} - (u^2 + v^2)_{\min}^{1/2} \\ C_{wk} &= 0.058 \end{aligned} \quad (2.30)$$

and Y_{\max} is the value of Y at which F_{\max} occurs. In the wake, Y is measured from the wake centerline as determined from the location of minimum velocity. The intermittency factor F_{kleb} is obtained from Equation (2.26) with $C_{\text{kleb}} = 0.53$. The constants C_{wk} and C_{kleb} are chosen in order to match the above formulation with the theoretical results given by Schlichting¹³ for an incompressible turbulent wake (see Appendix A for details).

The turbulent eddy viscosity in the near-wake ϵ_{nw} is computed by allowing the trailing edge eddy viscosity profile to exponentially reach its far-wake value. Referring to Figure 2, the following expression is employed

$$\epsilon_{nw}(x, Y) = \frac{1}{2} \left\{ \left[\epsilon(x_{te}, Y) + \epsilon_{wk}(x_0, Y) \right] + A \left[\epsilon_{wk}(x_0, Y) - \epsilon(x_{te}, Y) \right] \right\} \quad (2.31)$$

$$A = \tanh \left[8 \left(\frac{x - x_{te}}{x_0 - x_{te}} - \frac{1}{2} \right) \right]$$

The distance $x_0 - x_{te}$ is typically chosen to be of the order of 10δ , where δ denotes the average boundary layer thickness at the trailing edge. The sensitivity of the airfoil lift and drag coefficients to the variation of $x_0 - x_{te}$ is addressed in Section IV. This near-wake ad hoc formulation, similar to that of References 14 and 15, represents a preliminary approach within the context of a simple algebraic eddy viscosity model.

SECTION III NUMERICAL PROCEDURE

The numerical procedure consists of two basic steps. First, a body-fitted finite-difference grid, must be constructed about the airfoil in order to simplify the implementation of the boundary conditions and to provide sufficient resolution of the flow features. Second, the finite-difference form of the governing equations is solved using a suitable numerical scheme. In this investigation, grids were generated by the elliptic technique of Visbal and Knight.⁸ Two different schemes were utilized for the numerical solution of the flow equations. Namely, the implicit factored algorithm of Beam and Warming¹⁰, and the explicit unsplit MacCormack's algorithm.⁹ The grid generation method, the numerical schemes and the criterion for convergence of the solution to steady state are presented below.

1. GENERATION OF COMPUTATIONAL GRIDS

Nearly orthogonal body-fitted grids were generated about the airfoil using the method developed by Visbal¹⁶ and Visbal and Knight.^{8,17} This technique, which is based on elliptic partial differential equations¹⁸, employs the two-step procedure described below.

a. Intermediate Transformation

As a first step, an orthogonal grid is generated with a user-prescribed distribution of the mesh points along the airfoil and

wake-cut (Figure 1). The intermediate transformation $[\xi(x,y), x(x,y)]$ satisfies the Poisson equations¹⁶

$$\nabla^2 \xi = \xi_{xx} + \xi_{yy} = \phi(\xi, x) = \frac{1}{h_\xi h_x} \frac{\partial}{\partial \xi} \left(\frac{h_x}{h_\xi} \right) \quad (3.1)$$

$$\nabla^2 x = x_{xx} + x_{yy} = 0 \quad (3.2)$$

where

$$h_\xi = (x_\xi^2 + y_\xi^2)^{\frac{1}{2}} \quad (3.3)$$

$$h_x = (x_x^2 + y_x^2)^{\frac{1}{2}}$$

and the forcing function $\phi(\xi, x)$ results from the general expression for the Laplacian in orthogonal curvilinear coordinates. In reference to Figure 1, the boundary conditions for ξ and x are

$$\begin{aligned} \xi = 0, \quad \frac{\partial x}{\partial n} &= 0 && \text{on } \Gamma_1 \\ \xi = \xi_{\max}, \quad \frac{\partial x}{\partial n} &= 0 && \text{on } \Gamma_2 \\ \xi = \xi_3(t), \quad x &= 0 && \text{on } \Gamma_3 \\ \frac{\partial \xi}{\partial n} &= 0, \quad x = x_{\max} && \text{on } \Gamma_4 \end{aligned} \quad (3.4)$$

where t is the arc length along Γ_3 and n denotes the normal to the corresponding boundary. The boundary condition on Γ_3 simply indicates that the grid points are distributed along the airfoil and wake-cut in a desired monotonic fashion.

The transformation equations and boundary conditions (Equations (3.1) - (3.4)) are expressed in terms of (ξ, x) derivatives, as

shown in Reference 17. The resulting equations are solved for $[x(\xi, \chi), y(\xi, \chi)]$ in a uniform rectangular grid in the (ξ, χ) plane using point successive overrelaxation (SOR) and starting from an arbitrary (non-orthogonal) initial mesh. The forcing function ϕ and the grid points on Γ_1 , Γ_2 , Γ_4 are dynamically adjusted during the solution process.¹⁷

For the present airfoil grids, the above intermediate transformation technique is applied only in the vicinity of the airfoil (up to 2.-3. chords away). Since the grid is orthogonal, it can be easily extended to the outer boundary Γ_4 using a straight-forward algebraic procedure which results in an improved efficiency. In addition, a relatively coarse mesh in the χ direction can be utilized.

b. Final Transformation

In the second step, a nearly-orthogonal mesh is constructed with a user-specified distribution of grid points along Γ_1 and Γ_2 . The distribution along Γ_3 and Γ_4 is obtained from the intermediate mesh. Introducing the simple transformation $\chi = \chi(\eta)$, Equations (3.1) and (3.2) become¹⁷

$$\nabla^2 \xi = P(\xi, \eta) = \phi \left[\xi, \chi(\eta) \right] \quad (3.5)$$

$$\nabla^2 \eta = Q(\xi, \eta) = (\eta_x^2 + \eta_y^2)S \quad (3.6)$$

where

$$S = \begin{cases} T - y_\eta R / x_\xi & \text{if } x_\xi \geq y_\xi \\ T + x_\eta R / y_\xi & \text{if } x_\xi < y_\xi \end{cases} \quad (3.7)$$

$$R = (x_\xi y_{\xi\xi} - y_\xi x_{\xi\xi}) / (x_\xi^2 + y_\xi^2) \quad (3.8)$$

$$T = -(x_\eta x_{\eta\eta} + y_\eta y_{\eta\eta}) / (x_\eta^2 + y_\eta^2) = -s_{\eta\eta} / s_\eta \quad (3.9)$$

and s denotes the physical distance along the ξ -lines measured from Γ_3 (Figure 1a). The inverse final transformation equations and boundary conditions are described in detail in Reference 17. The forcing functions P and R are obtained from the intermediate grid using linear interpolation. The function T is determined for a given η -spacing through Equation (3.9). In this case, an exponential distribution of the η -lines is employed in order to resolve the airfoil boundary layers and wake. The resulting expression for T is

$$T = c_1(\xi) \quad (3.10)$$

where c_1 is determined at each ξ -location by specifying the normal mesh spacing next to the airfoil.¹⁶

A typical C-grid is shown in Figure 3. The mesh is nearly-orthogonal and displays substantial clustering in the viscous regions and in the airfoil leading and trailing edge areas. Additional applications of the present grid generation technique can be found in References 8, 16 and 17.

2. IMPLICIT NAVIER-STOKES CODE

The implicit code solves the strong conservative formulation of the Navier-Stokes equations [Equation (2.10)] using the approximate-factorization algorithm of Beam and Warming.¹⁰ This scheme in "delta" form and with first-order Euler time-differencing can be written as follows

$$\left\{ I + \Delta t \left[\frac{\partial A^n}{\partial \xi} - \frac{\partial^2 M^n}{\partial \xi^2} \right] \right\} \left\{ I + \Delta t \left[\frac{\partial B^n}{\partial \eta} - \frac{\partial^2 N^n}{\partial \eta^2} \right] \right\} \Delta \hat{q}^n = -\Delta t \left[\frac{\partial}{\partial \xi} (E_1 - V_1 - V_2)^n + \frac{\partial}{\partial \eta} (E_2 - W_1 - W_2)^n \right] \quad (3.11)$$

$$\hat{q}^{n+1} = \hat{q}^n + \Delta \hat{q}^n \quad (3.12)$$

where n denotes the temporal index (i.e. $\hat{q}^n = \hat{q} (n\Delta t)$), and the Jacobian matrices

$$A = \frac{\partial E_1}{\partial \hat{q}} \quad , \quad B = \frac{\partial E_2}{\partial \hat{q}} \quad (3.13)$$

$$M = \frac{\partial V_1}{\partial \hat{q}_\xi} \quad , \quad N = \frac{\partial W_2}{\partial \hat{q}_\eta}$$

are given in Appendix B.

Application of second order central differencing for the space derivatives yields

$$\left\{ I + \Delta t \left[\mu_\xi A_{i,j} - \delta_\xi^2 M_{i,j} \right] \right\} \Delta \hat{q}_{i,j}^* = -\Delta t \left[\mu_\xi (E_1 - V_2)_{i,j} + \mu_\eta (E_2 - W_1)_{i,j} - \delta_\xi V_1_{i,j} - \delta_\eta W_2_{i,j} \right] \quad (3.14)$$

$$\left\{ I + \Delta t \left[\mu_\eta B_{i,j} - \delta_\eta^2 N_{i,j} \right] \right\} \Delta \hat{q}_{i,j} = \Delta \hat{q}_{i,j}^* \quad (3.15)$$

where

$$\xi_i = (i - 1)\Delta\xi \quad , \quad 1 \leq i \leq IL \quad (3.16)$$

$$\eta_j = (j - 1)\Delta\eta \quad , \quad 1 \leq j \leq JL$$

and

$$\delta_\xi f_{i,j} = (f_{i+\frac{1}{2},j} - f_{i-\frac{1}{2},j})/\Delta\xi \quad , \quad \delta_\eta f_{i,j} = (f_{i,j+\frac{1}{2}} - f_{i,j-\frac{1}{2}})/\Delta\eta \quad (3.17)$$

$$u_\xi f_{i,j} = (f_{i+1,j} - f_{i-1,j})/2\Delta\xi \quad , \quad u_\eta f_{i,j} = (f_{i,j+1} - f_{i,j-1})/2\Delta\eta$$

are finite-difference operators. The transformation derivatives (x_ξ , x_η , y_ξ , y_η), required in Equations (3.14) and (3.15), are computed from the body-fitted grid using second-order central differences at interior points and one-sided approximations at the boundaries. The scheme is implemented in a standard ADI fashion by solving Equation (3.14) for each η -line ($2 \leq j \leq JL-1$), followed by the solution of Equation (3.15) for each ξ -line ($2 \leq i \leq IL-1$). This results in the solution of a block-tridiagonal linear system along every coordinate line.

In order to maintain numerical stability, artificial dissipative terms must be added to the basic Beam-Warming algorithm.¹⁰ Following Reference 19, explicit fourth-order damping

$$-\omega_e \Delta t J_{i,j}^{-1} (\delta_\xi^4 + \delta_\eta^4) q_{i,j}^n \quad (3.18)$$

is appended to the right-hand-side of Equation (3.14). The implicit second-order damping terms

$$-\omega_i \Delta t J_{i,j}^{-1} \delta_\xi^2 J_{i,j}^I, -\omega_i \Delta t J_{i,j}^{-1} \delta_n^2 J_{i,j}^I \quad (3.19)$$

are inserted within the respective implicit operators. The damping coefficient ω_e is of order one and $\omega_i \geq 2\omega_e$.

To accelerate convergence to steady-state the local time step $\Delta t_{i,j}$ is employed²⁰

$$\Delta t_{i,j} = \max \left[\Delta t_0, \frac{\sigma}{1 + \sqrt{J_{i,j}}} \right] \quad (3.20)$$

where σ is constant, typically from 1.0 to 2.0. For viscous flows, Δt_0 corresponds to a Courant number (CFL) of order 50-500 at the location of minimum grid spacing on the airfoil (see Equations (3.22)-(3.25) for the definition of the CFL number).

Finally, the boundary conditions are implemented in the explicit fashion described in Reference 12. A similar version of the present implicit code had been previously validated for a variety of flow configurations.²¹

3. EXPLICIT NAVIER-STOKES CODE

The explicit Navier-Stokes code solves the chain-rule conservative form of the governing equations (2.1) utilizing the explicit unsplit predictor-corrector algorithm of MacCormack.⁹ Details of this

well-known algorithm can be found in Reference 22 and therefore are not included here. As part of this scheme, a fourth-order pressure damping term is incorporated in order to control numerical oscillations in regions of large flow gradients. This damping term, used in both the predictor and corrector steps, has the form

$$D = D_{\xi} + D_{\eta}$$

$$D_{\xi} = -\beta \Delta t \Delta \xi^3 \frac{\partial}{\partial \xi} \left[(|u| + a|\vec{\Delta \xi}|) \frac{1}{4p} \left| \frac{\partial^2 p}{\partial \xi^2} \right| \frac{\partial q}{\partial \xi} \right] \quad (3.21)$$

$$D_{\eta} = -\beta \Delta t \Delta \eta^3 \frac{\partial}{\partial \eta} \left[(|v| + a|\vec{\Delta \eta}|) \frac{1}{4p} \left| \frac{\partial^2 p}{\partial \eta^2} \right| \frac{\partial q}{\partial \eta} \right]$$

where $a = \sqrt{\gamma R T}$ is the speed of sound, u, v are the contravariant velocities (Equation (2.16)) and β is the specified damping coefficient typically ranging from 1.0 to 3.0.

In order to improve the efficiency for steady flow computations, a local time step is incorporated in the basic MacCormack's algorithm. This is accomplished by specifying a constant Courant number (CFL) throughout the computational domain. Namely,

$$\Delta t_{i,j} = (CFL) \Delta t_{\max_{i,j}} \quad (3.22)$$

where

$$\Delta t_{\max_{i,j}} = \left[\frac{|u|}{\Delta \xi} + \frac{|v|}{\Delta \eta} + a \sqrt{\frac{1}{\Delta s_{\xi}^2} + \frac{1}{\Delta s_{\eta}^2}} \right. \\ \left. + \frac{2\gamma}{\rho} \frac{1}{\Delta s_{\eta}^2} \left(\frac{\mu}{p_r} + \frac{\epsilon}{p_{r_t}} \right) \right]^{-1} \quad (3.23)$$

$$\Delta s_{\xi} = (x_{\xi}^2 + y_{\xi}^2)^{\frac{1}{2}} \Delta \xi \quad (3.24)$$

$$\Delta s_n = (x_n^2 + y_n^2)^{1/2} \Delta n \quad (3.25)$$

The prescribed Courant number is typically assigned a value of 0.9.

Previous versions of this explicit Navier-Stokes code have been successfully applied to a variety of fluid dynamic problems.^{2,23} Unlike the implicit code which was written for a scalar computer, the explicit solver is fully vectorized and exploits the vector-processing capabilities of the CRAY computer.

4. STEADY-STATE CONVERGENCE CRITERION.

Since steady flowfields are obtained by time-integration of the Navier-Stokes equations from a given initial condition, a suitable convergence criterion must be specified. Convergence was assessed by carefully monitoring the airfoil lift (C_L) and drag (C_D) coefficients. For all cases computed, the monitored coefficients approached a steady value in a damped oscillatory fashion. Here, the flow was assumed converged when (1) the amplitude in the oscillations of C_L was less than 0.05 - 0.1% and (2) when the variations in C_D were within 1-2 drag counts (1 drag count = 0.0001). For the implicit algorithm, the corresponding root-mean-square values of the residual were typically 10^{-7} for all equations. Although, a more stringent convergence criterion could be stipulated, the present one was found to be suitable for engineering calculations.

5. CALCULATION OF AIRFOIL FORCE COEFFICIENTS

The airfoil lift and drag coefficients, denoted by C_L and C_D respectively, were computed by integration of the pressure and shear stress along the airfoil surface. The stress vector at the wall, f_k , is given in cartesian tensorial notation as follows

$$f_k = n_1 \sigma_{k1} \quad (3.26)$$

where

$$n_1 = \vec{\nabla} \eta / |\vec{\nabla} \eta|$$

is the normal to the surface and σ_{k1} is the stress tensor

$$\sigma_{k1} = \begin{pmatrix} \sigma_x & \tau_{xy} \\ \tau_{xy} & \sigma_y \end{pmatrix}$$

where $\sigma_x = -p + \tau_{xx}$, $\sigma_y = -p + \tau_{yy}$ and τ_{xx} , τ_{xy} , τ_{yy} are given in Equations (2.4). Performing the tensorial inner product (3.26) and assuming $u = v = 0$ and $\epsilon = 0$ at the surface, one obtains

$$f_x = \frac{n_x}{|\vec{\nabla} \eta|} \left[-p + \frac{1}{3} \mu (n_x u_\eta + n_y v_\eta) \right] + |\vec{\nabla} \eta| \mu u_\eta \quad (3.27)$$

$$f_y = \frac{n_y}{|\vec{\nabla} \eta|} \left[-p + \frac{1}{3} \mu (n_x u_\eta + n_y v_\eta) \right] + |\vec{\nabla} \eta| \mu v_\eta \quad (3.28)$$

where f_x , f_y represent the stress components in the x and y directions respectively.

The total force on the airfoil per unit span (F_x , F_y) is obtained by straight-forward integration

$$F_x = \oint f_x ds, \quad F_y = \oint f_y ds$$

using trapezoidal rule. Finally, the lift and drag coefficients are given by

$$C_L = (-F_x \sin \alpha + F_y \cos \alpha) / \frac{1}{2} \rho_\infty U_\infty^2 \quad (3.29)$$

$$C_D = (F_x \cos \alpha + F_y \sin \alpha) / \frac{1}{2} \rho_\infty U_\infty^2 \quad (3.30)$$

where α is the airfoil angle of attack.

SECTION IV
RESULTS AND DISCUSSION

1. FLOW CONFIGURATION AND COMPUTATIONAL DETAILS

Computations were performed for an 11% thick supercritical airfoil designated as DSMA 523.⁴ This modified Whitcomb airfoil exhibits significant rear-loading and a strong viscous-inviscid interaction as compared to more conventional sections having little or no aft-camber. This particular airfoil was selected as one of the test cases for the 1980 Stanford Conference on Complex Turbulent Flows.⁵ The experimental database⁴ contains surface pressure distributions and velocity and density profiles along the upper surface, lower surface and wake for a range of Mach number, Reynolds number and angle of attack. Two specific cases were considered in this study. Namely, a subcritical case ($M_\infty = 0.6$, $\alpha = 2.6^\circ$, $Re_c = 4 \times 10^6$) and a supercritical case ($M_\infty = 0.8$, $\alpha = 1.8^\circ$, $Re_c = 2 \times 10^6$). The corresponding flow parameters are given in detail in Table 1.

In the calculations, three different computational grids were employed. These grids, referred to subsequently as coarse (92 x 31), medium (140 x 45) and fine (204 x 55), were generated by the procedure described in Section III. As shown in Figure 3 for the fine grid, the mesh is nearly orthogonal and displays substantial clustering in regions of high flow gradients. The details of all grids are summarized for convenience in Table 2.

Numerical solutions of the flow equations were obtained utilizing either the explicit unsplit MacCormack's scheme or the implicit Beam-Warming algorithm. Both schemes incorporated a local Δt (Equations (3.20) and 3.22)) in order to accelerate convergence to steady state. The effect on convergence when using a local Δt was investigated for both algorithms and is discussed next.

Computations for the airfoil subcritical case on the coarse grid using Beam-Warming algorithm indicated a gain in efficiency of about six when a local Δt was employed (with $\Delta t_0 = 0.01$, $\sigma = 0.5$ in Equation (3.20)). The convergence history for the airfoil lift and drag coefficients is shown in Figure 4 and points out that an unphysical oscillatory solution can occur for higher values of σ and Δt_0 . However, when a steady state was reached, the results were as expected independent of σ and Δt_0 .

MacCormack's code with a local Δt displayed a speed-up factor of approximately seven for the computation of a flat plate supersonic ($M_\infty = 3.0$) boundary layer with mass injection. Figure 5 shows the convergence of the skin friction coefficient at a given location. When applied to the airfoil, the use of a local Δt resulted in small amplitude oscillations about the steady solution (see Figure 6). These oscillations disappeared when a constant Δt was imposed. Despite this behaviour, using a local Δt during the early stages of the calculation substantially improved the efficiency of the explicit algorithm.

TABLE 1. FLOW PARAMETERS

Case	M_∞	Re_c	α	x/c transition		Experimental	
				upper	lower	C_L	C_D
Subcritical	0.6	4×10^6	2.6°	0.05	0.18	0.58	0.011
Supercritical	0.8	2×10^6	1.8°	0.35	0.18	0.65	0.017

TABLE 2. GRID DETAILS

Grid	IL x JL	$\Delta s_\xi/c$		$\Delta s_\eta/c$		No. of points on airfoil	$M_\infty = 0.6$	$M_\infty = 0.8$
		min.	max.	min.	max.			
1	92 x 31	0.010	0.060	0.00025	1.03	58	18.5	--
2	140 x 45	0.005	0.050	0.00010	1.38	86	11.5	--
3	204 x 55	0.003	0.025	0.00005	1.25	150	6.9	2.1

Legend

IL, JL : No. of grid points in ξ and η directions respectively.
 Δs_ξ : streamwise grid spacing on airfoil (Equation (3.24))
 Δs_η : grid spacing normal to airfoil surface (Equation (3.25))
 Δs_2^+ : normal spacing at airfoil surface in terms of law of
 the wall coordinates (upper surface, $x/c = 0.5$)

NOTE: For the above grids, the farfield boundary was located 10 chords away from the airfoil.

The airfoil calculations were performed on a CYBER 175 and on the NASA Ames CRAY XMP computer. The average rates of data processing, defined as CPU time per grid point per iteration, are given in Table 3 for both algorithms. The efficiency increase on the CRAY XMP relative to the CYBER 175 was a factor of 55 for the vectorized explicit code. However, the corresponding value for the scalar implicit algorithm was only a factor of 5.1. For a typical airfoil steady solution on a 204 x 55 grid, the implicit code was about 3.8 times faster than the explicit code on the scalar computer. However, the situation was reversed on the vector computer, with the explicit code being 2.9 times faster. It should be noted, however, that the efficiency of the implicit algorithm could be increased substantially by vectorization and by the techniques of References 24 and 25.

A total of 23 different calculations were performed for the selected airfoil configuration. A detailed comparison of numerical results and experiments is presented below for the subcritical and supercritical case separately.

TABLE 3.
COMPARISON OF COMPUTER TIMES FOR EXPLICIT
AND
IMPLICIT CODES

Algorithm	DPR ^a CYBER 175	DPR ^a CRAY XMP	Approx. No. of Iterations req'd for convergence ^b	Overall relative speed ^b CYBER 175	Overall relative speed ^b CRAY XMP
BEAM-WARMING	4.4×10^{-3}	8.6×10^{-4}	900	3.8	0.35
MACCORMACK	0.6×10^{-3}	1.1×10^{-5}	25,000	1.0	1.0

(a) DPR: Data processing rate, $\frac{\text{CPU (sec)}}{(\text{No. of grid points})(\text{No. time steps})}$

(b) For 204 x 55 grid

2. RESULTS FOR SUBCRITICAL CASE

Since in the experiments⁴ the ratio of wind tunnel height to model chord was only four, interference effects are expected to be significant and must be accounted for (assuming the data is correctable) by adjustments in the freestream Mach number and angle of attack. Although the main objective of the present study is the comparison of the two numerical schemes, an attempt was made to determine the effective angle of attack for the subcritical case in order to provide a more meaningful comparison with the experiments. For this purpose, several computations were performed with the implicit code on the coarse grid at various angles of attack. The C_p -distribution and lift coefficients, shown in Figure 7, indicated an effective angle of attack (α) of approximately 1.7 degrees in order to match the experimental C_L . All subsequent calculations were therefore performed with this value of α .

The sensitivity of the numerical solution to the relaxation length $x_0 - x_{te}$ in the near wake turbulence model (Equation (2.31)) was investigated next. The flow was computed with the implicit algorithm using two values of $x_0 - x_{te}$ differing by an order of magnitude (namely, 0.2c and 2.0c where c is the airfoil chord length). As Figure 8 shows, the solution was insensitive to variations in the near-wake relaxation distance. In the remaining calculations, the value $x_0 - x_{te} = 0.2c$ was therefore employed. This value is approximately 8δ , where δ denotes the average boundary layer thickness at the airfoil trailing edge.

According to a formal truncation error analysis, the numerical smoothing terms are of high order and therefore their effects on the accuracy of the numerical solution are seldom considered. In the present

study, the effects of artificial viscosity on the computed airfoil viscous flowfield were investigated on a limited basis. Calculations were carried out on the coarse mesh using both codes and different damping coefficients. The results for C_p , C_L and C_D are given in Figure 9. The variations of C_p with damping were slightly larger for Beam-Warming algorithm (Figure 9a) as compared to MacCormack's scheme (Figure 9b). In both cases, the lift coefficient remained essentially unchanged while C_D varied by as much as 30 drag counts. Since the effects of damping are expected to diminish as the mesh resolution increases, computations were performed on the fine grid using MacCormack's algorithm with two values for the damping coefficient differing by a factor of three. The corresponding variations in C_L and C_D with the damping coefficient were 0.3% and eight counts respectively.

In order to investigate the effects of numerical resolution, the flowfield was computed on all three grid systems (Table 2) using both Navier-Stokes codes. The results for the implicit algorithm are displayed in Figure 10. The computed lift coefficient increased monotonically with increasing resolution unlike the drag coefficient which did not show any specific trend. The variations in C_L and C_D through the second mesh refinement were only 2.2% and 5 drag counts respectively as compared to 12% and 19 counts for the first grid refinement. Although some measure of numerical convergence is observed, the C_p -distributions (Figure 10) indicate that further resolution on the upper surface leading edge area is still required. Figure 11 shows the Mach number contours near the relatively blunt leading edge for the coarse and fine grids. Besides being much more smooth, the fine grid

solution makes apparent the existence of an embedded supersonic region (terminated by a shock) at the leading edge. The corresponding mesh refinement results for the explicit scheme, shown in Figures 12 and 13, displayed a behaviour similar to that of the implicit algorithm. For the explicit code, the variations in C_L and C_D after the second grid refinement were 1.0% and 15 drag counts respectively.

A comparison between MacCormack and Beam-Warming results as well as between the computed results and the experiments is presented below. Figures 14, 15 and 16 contain the results for C_p , C_L and C_D on the coarse, medium and fine grids respectively. The agreement between the two calculated C_p -distributions improves as the mesh is refined. However, differences still persist on the airfoil upper surface immediately downstream of the embedded supersonic region. The computed lift and drag coefficients obtained with the two algorithms on the fine grid (Figure 16) differ by 1.8% and 5 drag counts respectively. These discrepancies are acceptable for engineering applications. The better agreement (in terms of C_L and C_D) between the two numerical schemes on the coarse mesh (Figure 14) can only be regarded as fortuitous.

In order to illustrate the importance of viscous effects for supercritical airfoils, the inviscid flowfield was computed with the implicit code on the coarse (Figure 14) and medium (Figure 15) grids. Even for a small angle of attack, subcritical flow without significant boundary layer separation, the decrease in C_L due to viscous effects is substantial (approximately 29% for the medium-grid solution, Figure 15).

Referring to Figure 15, the discrepancies in C_p and C_L between the fine-grid computational results and the experiments are in part due

to uncertainties in the effective freestream Mach number and angle of attack. The better prediction of the experimental lift coefficient on the coarse mesh (Figure 14) simply points out that comparison with experimental data can be misleading unless proper numerical resolution criteria are first established.

A detailed comparison of computed and experimental velocity profiles is given in Figures 17 - 19 for the airfoil upper surface, lower surface and wake. As expected, the numerical profiles obtained with the explicit and implicit codes are in very good agreement with each other at all locations. On the suction surface (Figure 17), the predicted profiles show higher values for the freestream velocity. This is consistent with the higher computed C_L (Figure 16) and can be attributed mainly to uncertainties in the effective angle of attack. The discrepancies between the measured and computed velocity profiles at the airfoil cove (Figure 18) and in the near-wake (Figure 19) are most likely due to deficiencies in the algebraic turbulent eddy viscosity model employed.

A qualitative comparison of computed density contours and the experimental interferogram is presented in Figure 20. All typical features of the subcritical flow about the airfoil are discernible and in good qualitative agreement with the experimental, flowfield. A close-up comparison near the trailing edge is shown in Figure 21.

It is interesting to compare the uncertainties in the numerical simulation of different algorithms with the experimental uncertainties associated with different wind tunnel occupancy periods.⁴ Figure 22a shows two measured C_p -distributions for the same nominal subcritical

conditions. The specific comparison indicates that the experimental uncertainty is of the same order of magnitude as the discrepancies between the two numerical algorithms (Figure 16).

3. RESULTS FOR SUPERCRITICAL CASE

Calculations for the supercritical flow case (Table 1) using both numerical algorithms were limited to the fine grid (Table 2). The coarser grid systems are not expected to provide sufficient spatial resolution.

In order to achieve a more meaningful comparison between computations and experiments, an attempt was made to determine the effective freestream Mach number and angle of attack. As shown in Figure 23, computations at the nominal conditions ($M_\infty = 0.8$, $\alpha = 1.8^\circ$) predicted a shock location much further aft as compared to the experimental data. The freestream Mach number $M_\infty = .765$ and angle of attack $\alpha = 0.7^\circ$ were found to approximate the experimental shock position. These values were therefore employed in all subsequent calculations. As suggested in Reference 5, the experimental C_p and C_L were corrected to account for the shift in Mach number by keeping a constant static-to-total pressure ratio. The present computations indicated that this supercritical airfoil is extremely sensitive to small variations in the freestream Mach number.

Since the farfield boundary conditions employed in this study are only approximate (see Section II), the effect of the outer boundary placement on the numerical solution must be investigated. For this purpose, the supercritical flowfield was computed with the explicit algorithm for three different locations of the farfield boundary (namely, 10, 25 and 50 chords away). The results for C_p , C_L and C_D are

shown in Figure 24 and indicate that as the outer boundary is placed further away from the airfoil the shock moves downstream with a corresponding increase in lift. The difference in C_L between the 25 chord and 50 chord solution is only 1.8%. Although additional outward boundary placements have not been considered, it may be concluded that a computational domain extending at least 50 chords away from the airfoil should be employed for strong viscous-inviscid interacting calculations. The farfield boundary effects might be less significant for more conventional airfoils or for improved formulations of the boundary conditions.

A comparison of the computed results and experiments is presented below. Figure 25 displays reasonable agreement between the two numerical C_p -distributions except in the vicinity of the shock where additional spatial resolution in the streamwise direction is still needed. Both computed solutions failed to predict the measured static pressure on the upper surface downstream of the shock and on the lower surface cove. It appears that this discrepancies point out deficiencies in the algebraic turbulence model downstream of the shock-boundary-layer interaction and in the cambered region. A comparison of the velocity profiles on the upper surface, lower surface and wake is given in Figures 26, 27 and 28 respectively. The computed velocities are, as expected, in close agreement with each other. Discrepancies between the experimental and computed velocity profiles in the cove and near-wake are apparent. Finally, a qualitative comparison of the experimental and numerical flowfields is presented in Figure 29 in terms of computed density contours and the experimental interferogram.

It is interesting to compare the uncertainties in the numerical results of different algorithms with the repeatability in the experimental measurements. Figure 22b, reprinted from Reference 4, shows the pressure distributions obtained for the same nominal conditions during two different wind tunnel runs. For this case, the experimental uncertainty is found to be of the same order of magnitude as that encountered in the numerical simulation (Figure 25).

The thin-layer approximation (Equation (2.20)) has been commonly employed in the numerical solution of high Reynolds number airfoil flows,²⁶ and justification for its use can be found in Reference 7. For unsteady transonic airfoils, significant discrepancies between the thin-layer and the full Navier-Stokes results were observed by Chyu and Kuwahara.²⁷ On the other hand, Degani and Steger²⁸ found good agreement between the two formulations when applied to a supersonic compression ramp. In the present study, the effect of the thin-layer approximation was investigated for the airfoil supercritical flow. The results, shown in Figure 31, indicated very good agreement between the thin-layer and the full Navier-Stokes solution. Therefore, the use of the thin-layer equations is fully justified for this particular type of flows.

To illustrate the extent of the viscous-inviscid interaction effects for aft-cambered airfoils, the flowfield was also computed using the Euler equations. As Figure 31 shows, the presence of the boundary layer modifies the flowfield dramatically. Viscous effects result in a much weaker shock (displaced upstream) and in a substantial decrease in the "plateau" loading. This is a direct consequence of boundary layer

displacement effects which reduce the effective airfoil aft-camber. The viscous lift coefficient is almost half of the corresponding inviscid value.

4. INVESTIGATION OF NUMERICAL ERROR DUE TO DAMPING

In the previous sections, the effects of different numerical schemes, grid resolution, damping coefficient and farfield boundary placement were described. An additional assessment of the accuracy of the computed solutions was performed by evaluating the amount of numerical damping relative to the formal truncation error and by comparison of the physical and artificial viscosities.

For the strong conservative form implicit algorithm [Equation (3.18)], the magnitude of the numerical damping relative to the formal truncation error leading term can be evaluated as follows.

$$\left| \omega_e^J (\delta_\xi^4 + \delta_n^4) q \right| \leq \left| \frac{1}{6} (\hat{F}_{\xi\xi\xi} \Delta\xi^2 + \hat{G}_{nnn} \Delta n^2) \right| \quad (4.1)$$

The corresponding expression for the explicit algorithm is

$$\left| \frac{J^{-1}}{\Delta t} (D_\xi + D_n) \right| \leq \left| \frac{1}{6} (\hat{F}_{\xi\xi\xi} \Delta\xi^2 + \hat{G}_{nnn} \Delta n^2) \right| \quad (4.2)$$

where D_ξ and D_n are given by Equation (3.21). If the numerical solution is not to be seriously degraded by damping, the above expressions must be smaller than or equal to one. In other words, the smoothing terms must be of higher order as compared to the formal truncation error.

The damping-to-truncation error ratio was evaluated for the computed solutions using Equations (4.1) and (4.2), and the results for

the continuity equation are given in Table 4 (the results for the remaining equations were found to be similar). The root-mean-square value of the damping relative magnitude was always less than one. However, the maximum value was an order of magnitude greater. A contour plot of the damping-to-truncation error ratio (Equation (4.2)) for the continuity equation is shown in Figure 31 for the supercritical case. Only contour values greater than one were drawn for clarity. As expected, the region of large error is located in the vicinity of the shock, where the accuracy of the solution is already degraded.

A second assessment of the numerical error due to damping was performed by comparing the artificial viscosity, introduced by the smoothing terms, with the real physical viscosity $\mu + \epsilon$. This was done for the explicit algorithm due to the particular form of the damping terms (Equation (3.21)). Comparison of the damping term D_η with the normal diffusive terms in the streamwise momentum equation (Equations (2.1) - 2.4)) yields the following approximate expression for the artificial-to-real viscosity ratio.

$$\frac{\mu_{\text{artificial}}}{\mu + \epsilon} = \frac{\beta(|V| + a |\nabla \eta|) \frac{1}{4P} \frac{\partial^2}{\partial \eta^2} |\rho \Delta \eta^3|}{|\nabla \eta|^2 (\mu + \epsilon)} \quad (4.3)$$

Contours of the above ratio are shown in Figure 32 for both the subcritical and supercritical case. It can be seen than within the airfoil viscous region the artificial viscosity is one order of magnitude smaller than the true viscosity $\mu + \epsilon$. A similar analysis can be performed for the ξ -direction damping term D_ξ . This term was only found to be significant for the supercritical case in the vicinity of the shock where D_ξ becomes comparable in magnitude to the normal diffusive term.

The above results can only be regarded as a preliminary attempt to assess, *a posteriori*, the accuracy of the computed flowfields, and further grid refinement still represents the only conclusive approach for determining appropriate numerical resolution criteria.

TABLE 4. DAMPING-TO-TRUNCATION ERROR RATIO
FOR THE CONTINUITY EQUATION

	Explicit Algorithm		Implicit Algorithm	
	max.	rms	max.	rms
SUBCRITICAL CASE	29.1	0.47	7.1	0.25
SUPERCritical CASE	28.1	0.48	10.0	0.46

SECTION V

CONCLUSIONS AND RECOMMENDATIONS

In the present study, a critical examination of the numerical solution of high Reynolds number transonic airfoils was performed. Solutions of the flowfield about a supercritical airfoil were generated by solving the two-dimensional Navier-Stokes equations with an algebraic turbulent eddy viscosity model. The governing equations were solved on curvilinear body-fitted grids using two different numerical algorithms. Namely, the explicit unsplit MacCormack's scheme and the implicit Beam-Warming algorithm. Both subcritical and supercritical flows were considered, with a total of 23 cases computed.

The numerical uncertainties associated with different schemes, grid resolution, artificial viscosity and farfield boundary placement were carefully examined. Numerical simulations produced by the two numerical schemes with different conservative formulations exhibited nearly identical velocity profiles and density contours. The maximum discrepancy between these solutions was generally less than the repeatable data scattering band of experimental measurements. However, the uncertainty in the more stringent requirement of the computed lift and drag coefficient is still of the order of 2.0 and 20 drag counts respectively for the finest grid (204 x 55) utilized. Further numerical resolution, particularly in shock regions, is still required. This could perhaps be achieved, in a more efficient manner, by the use of grid adaptation techniques.

A comparison of the supercritical flowfields obtained with the Euler, thin-layer and Navier-Stokes equations was performed. The thin-layer approximation gave essentially the same results as the full Navier-Stokes equations and therefore its use, for this type of flows, is clearly justified. However, numerical solutions of the Euler equations failed to provide a reasonable approximation of the flowfield due to the dramatic viscous/inviscid interaction effects for transonic aft-cambered airfoils.

Comparison of the computed results and the experimental data showed a reasonable prediction of all of the essential features of the flow. However, detailed comparison of velocity profiles on the airfoil upper surface lower surface and wake pointed out deficiencies of the turbulence model in the cove region, downstream of the shock/boundary layer interaction and in the near-wake.

The comparison of computed and experimental results was clouded by uncertainties in both the measurements and in the numerical procedure. In principle, the numerical uncertainties could be reduced to a desired acceptable level. However, the uncertainties in the measurements were not adequately documented in the experimental study. For the investigated supercritical airfoil, the problem is significant due to the extreme sensitivity of the flow to variations in the freestream Mach number and angle of attack. Therefore, before a conclusive evaluation of turbulence modeling can be conducted, an experimental study aimed at the determination of interference effects should be performed. An alternative and less expensive approach of evaluating interference effects would be the numerical simulation of the entire three-dimensional wind-tunnel flowfield.

APPENDIX A
CONSTANTS FOR FAR-WAKE TURBULENCE MODEL

The similarity velocity profile in a two-dimensional incompressible turbulent wake can be expressed as follows¹³

$$U_{\max} - U = U_{\text{DiF}} \exp(-\eta^2) \quad (\text{A.1})$$

where

$$\eta = 1/2 \left(\frac{\rho U_{\infty}}{\epsilon_0} \frac{x}{x} \right)^{1/2} \gamma$$

$$U_{\text{DiF}} = U_{\max} - U_{\min} = 6.3535 \left(\frac{U_{\infty} \epsilon_0}{\rho x} \right)^{1/2}$$

ϵ_0 is the turbulent eddy viscosity and U_{\max} ($= U_{\infty}$) and U_{\min} are the maximum (freesream) and minimum velocities, respectively.

Assuming $|\omega| \sim |\partial U / \partial Y|$ in Equation (2.30), and using Equation (A.1) for the velocity, it can be easily shown that

$$F = 2U_{\text{DiF}} \eta^2 \exp(-\eta^2) \quad (\text{A.2})$$

$$F_{\max} = 0.7358 U_{\text{DiF}}$$

and

$$\gamma_{\max} = 2 \left(\frac{\epsilon_0 x}{\rho U_{\infty}} \right)^{1/2} \quad (\text{A.3})$$

Substituting the expressions for U_{DIF} , F_{max} and Y_{max} in Equation (2.29) and temporarily dropping the term F_{kleb} , for convenience, yields the following expression for the far-wake eddy viscosity

$$\varepsilon_{wk} = \frac{C_{wk}}{0.0579} \varepsilon_0$$

Therefore, in order to have $\varepsilon_{wk} = \varepsilon_0$, the constant C_{wk} must be set equal to 0.0579.

For the wake, the constant C_{kleb} appearing in Equation (2.28) is determined as follows

$$C_{kleb} = \frac{Y_{max}}{b}$$

where b is the wake half-width¹³

$$b = 3.798 \left(\frac{\varepsilon_0 X}{\rho U_\infty} \right)^{1/2}$$

and Y_{max} is given in Equation (A.3). The resulting value for C_{kleb} is 0.527.

APPENDIX B
JACOBIAN MATRICES FOR THE NAVIER-STOKES EQUATIONS

The Jacobian matrices defined in Equation (3.13) are given below. These matrices are obtained by straight-forward differentiation, after rewriting the vectors E_1 , E_2 , V_1 , W_2 (Equations (2.11) - (2.15)) in terms of the conserved variables (ρ/J , $\rho u/J$, $\rho v/J$, $\rho e/J$). The Jacobian matrix A is

$$A = \begin{pmatrix} 0 & \xi_x & \xi_y & 0 \\ \xi_x \phi - u u & u(\gamma-2) \xi_x u & -(\gamma-1) \xi_x v + \xi_y u & (\gamma-1) \xi_x \\ \xi_y \phi - v u & \xi_x v - (\gamma-1) \xi_y u & u - (\gamma-2) \xi_y v & (\gamma-1) \xi_y \\ (2\phi - \gamma e) u & (\gamma e - \phi) \xi_x - (\gamma-1) u u & (\gamma e - \phi) \xi_y - (\gamma-1) v u & \gamma u \end{pmatrix} \quad (B.1)$$

where

$$\phi = 1/2 (\gamma-1) (u^2 + v^2)$$

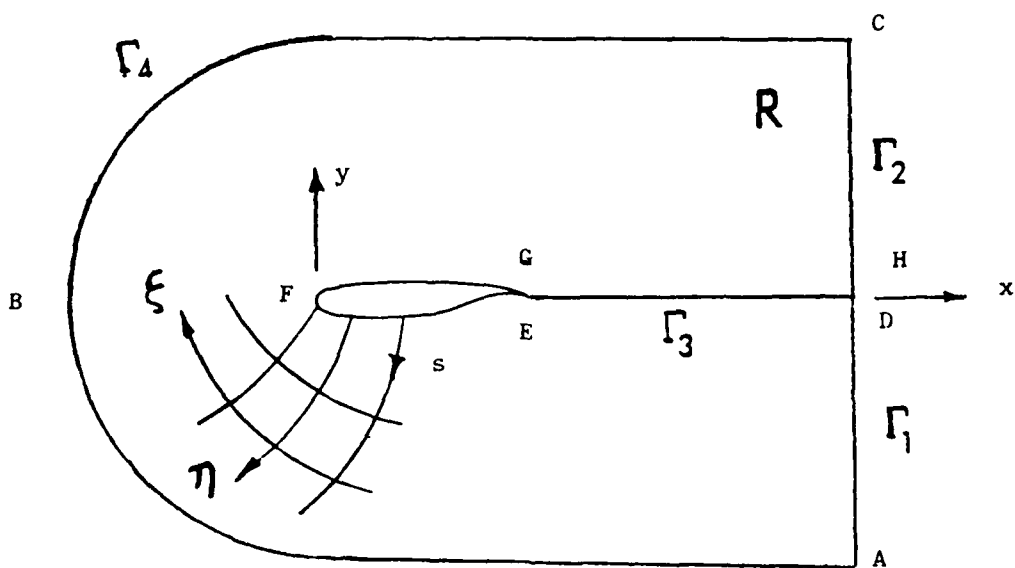
and u is given in Equation (2.16). The Jacobian matrix B can be obtained from Equation (B.1) by applying the substitutions

$$\begin{aligned} v &\rightarrow u \\ n_x &\rightarrow \xi_x \\ n_y &\rightarrow \xi_y \end{aligned}$$

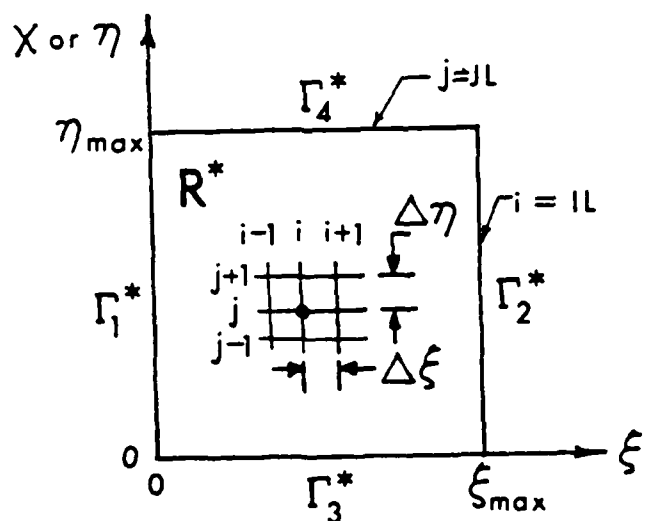
The Jacobian matrix M is

$$M = \frac{1}{\rho} \begin{pmatrix} 0 & 0 & 0 & 0 \\ -(b_1 u + b_2 v) & b_1 & b_2 & 0 \\ -(b_2 u + b_3 v) & b_2 & b_3 & 0 \\ -(b_1 u^2 + 2b_2 uv + b_3 v^2) & b_1 - b_4 \gamma(\gamma - 1) u & b_2 u + b_3 & b_4 \gamma(\gamma - 1) \\ + b_4 \gamma(\gamma - 1)(u^2 + v^2 - e) & +b_2 v & -b_4 \gamma(\gamma - 1) v & \end{pmatrix} \quad (B-2)$$

where the coefficients b_i ($i = 1, \dots, 4$) are given in Equation (2.17). The Jacobian matrix N can be obtained from Equation (B.2) by replacing the coefficients b_i with the corresponding coefficients d_i (Equation (2.19)).



(a) Physical Plane



(b) Transformed Plane

FIGURE 1 Basic Transformation

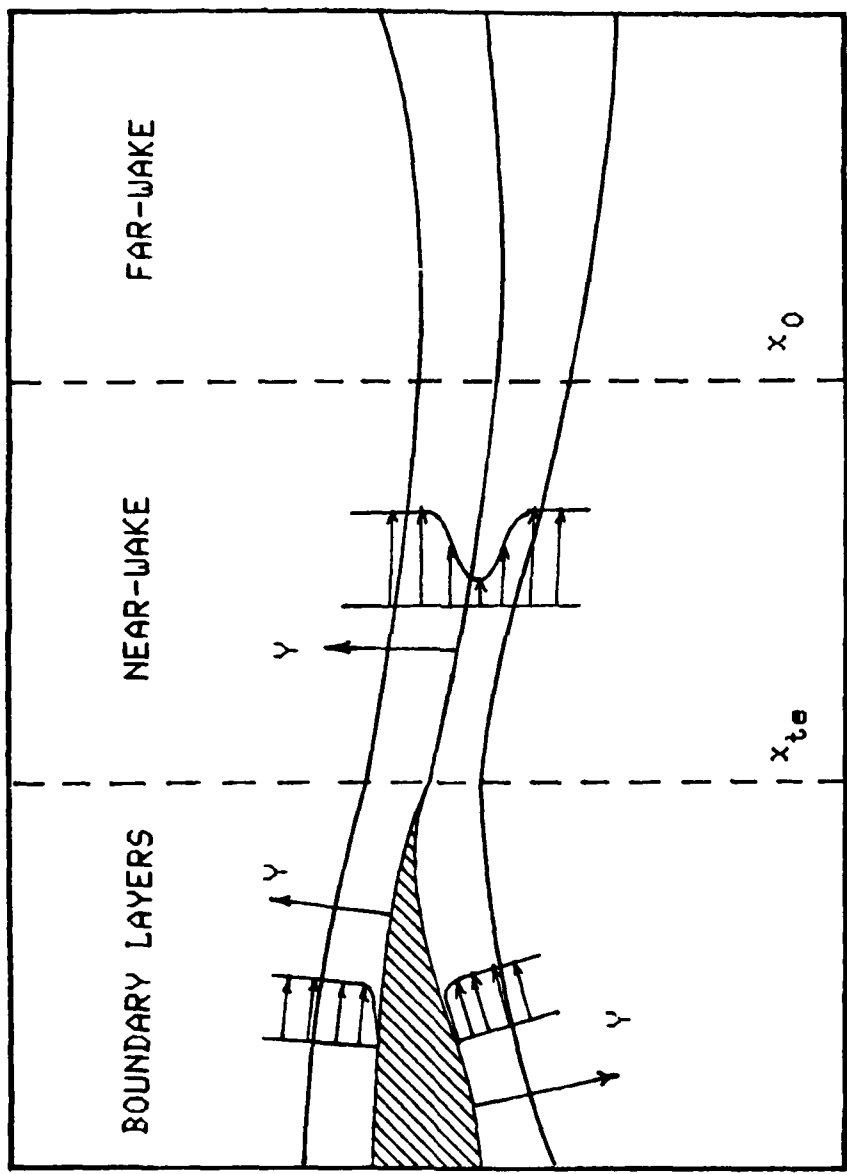
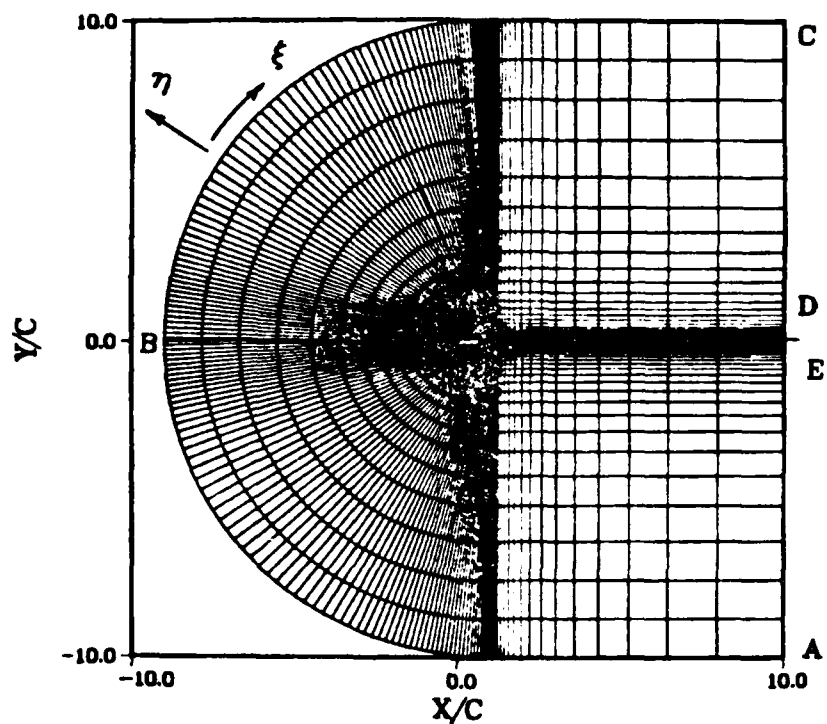
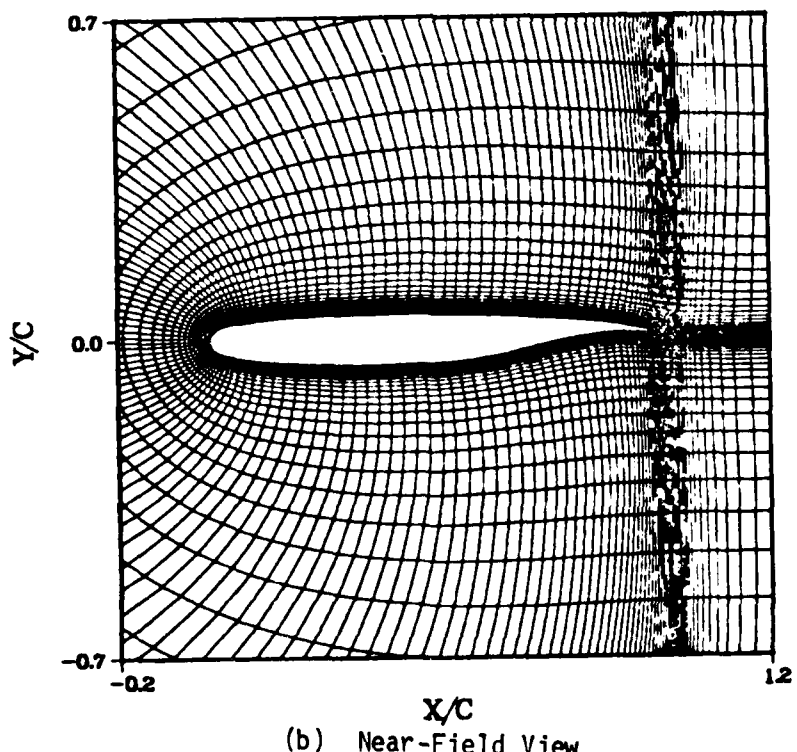


FIGURE 2 Regions for Turbulence Model 1



(a) Overview



(b) Near-Field View

FIGURE 3 Boundary - Fitted Grid

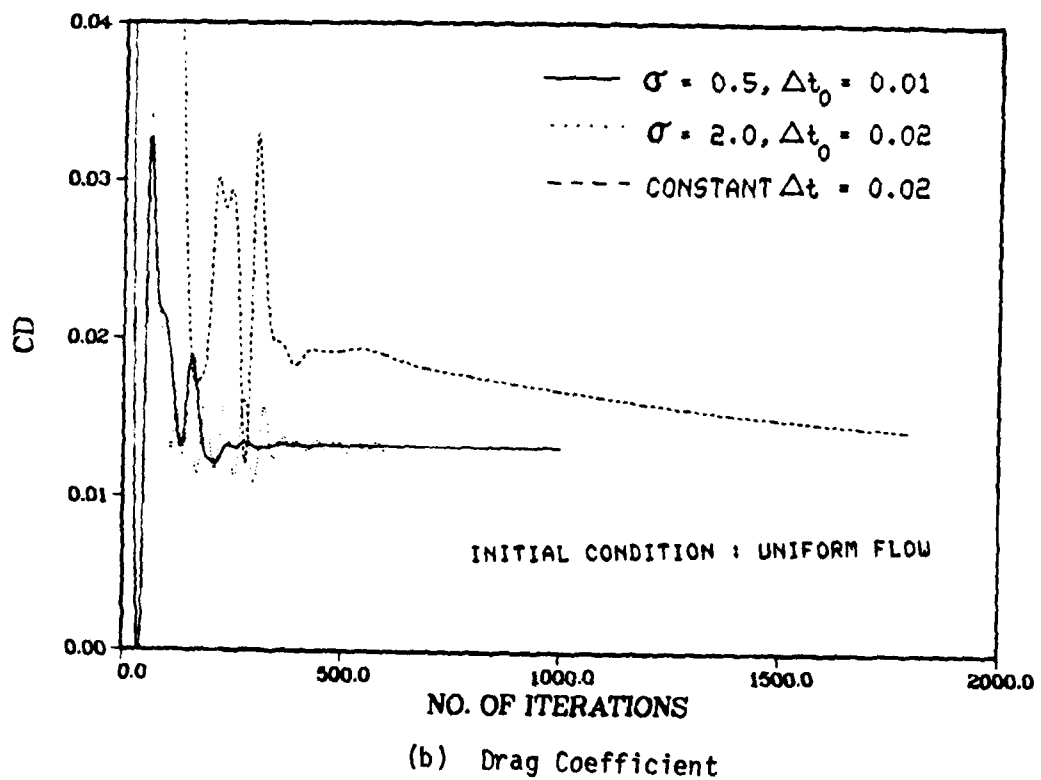
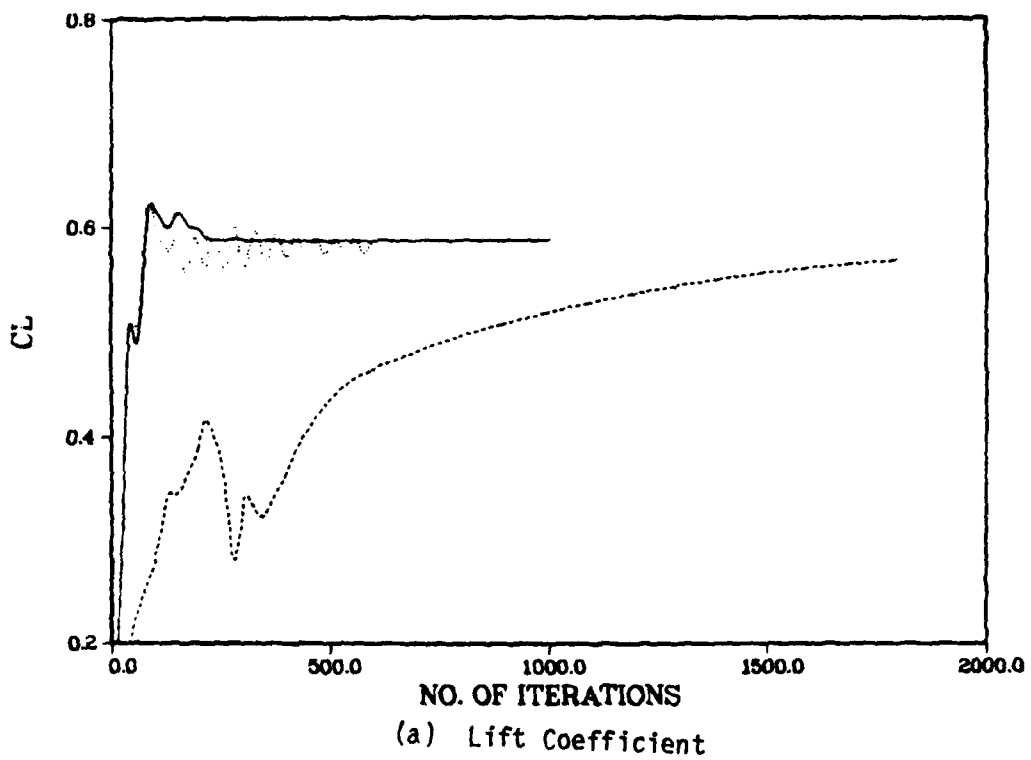


FIGURE 4 Convergence of C_L and C_D for Implicit Code
 (Airfoil Subcritical Case, Coarse grid)

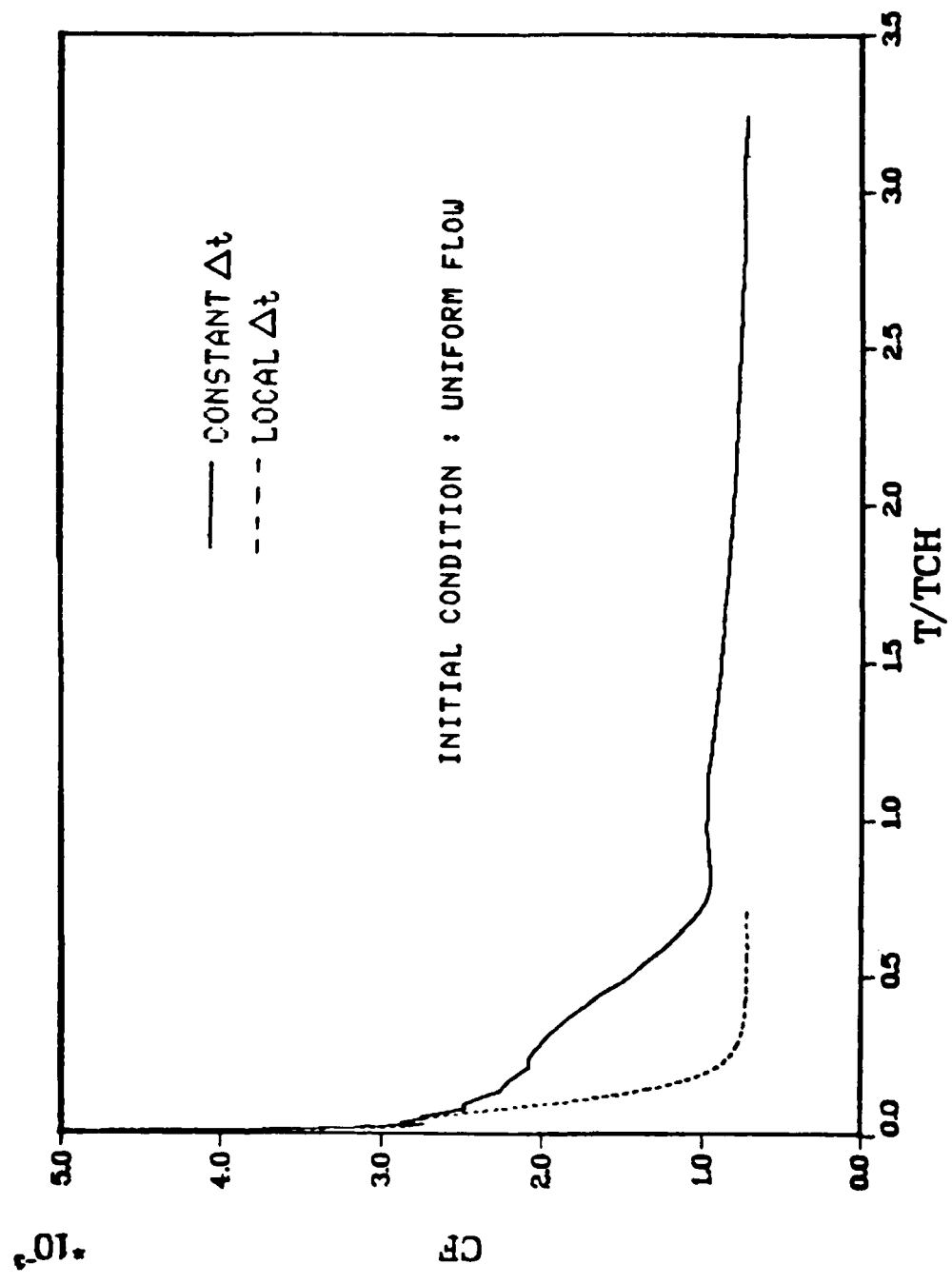


FIGURE 5 Convergence of Skin Friction Coefficient for Explicit Code
(Supersonic Flat Plate Boundary Layer with Blowing)

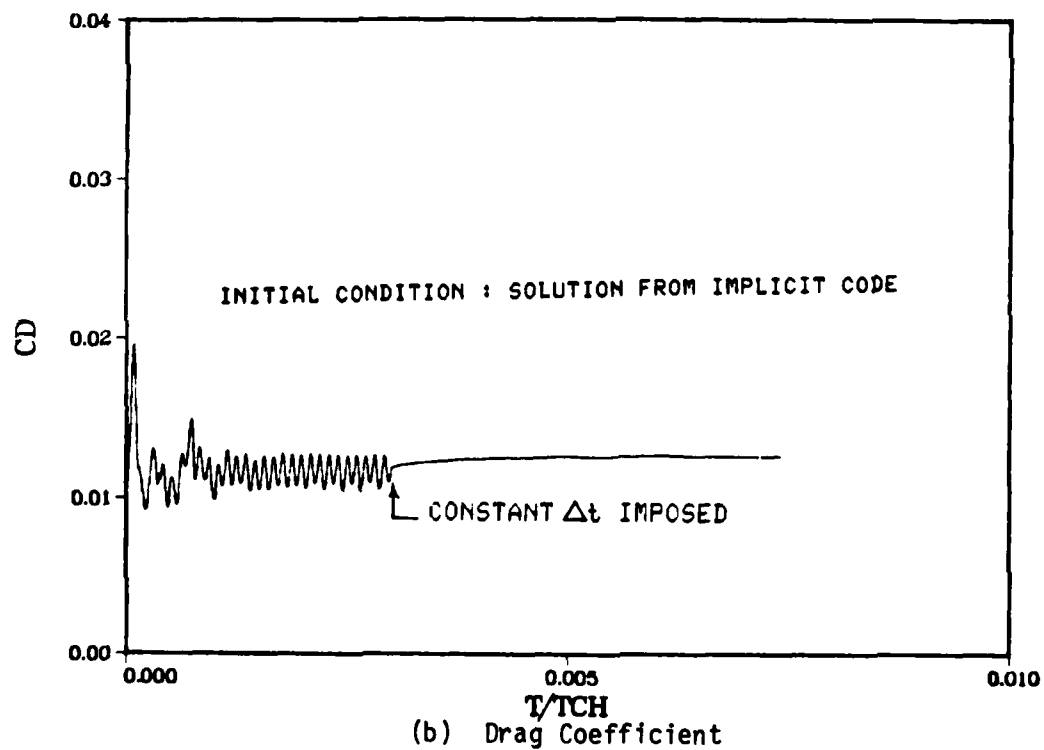
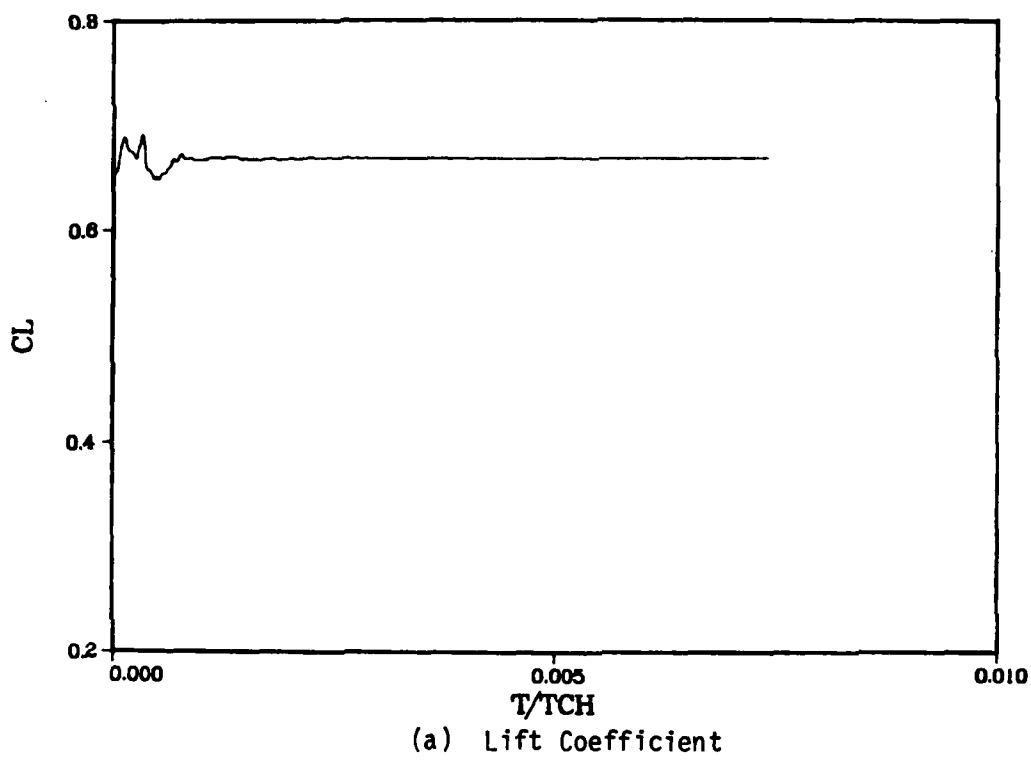


FIGURE 6 Convergence of C_L and C_D for Explicit Code
(Airfoil Subcritical Case, Fine Grid)

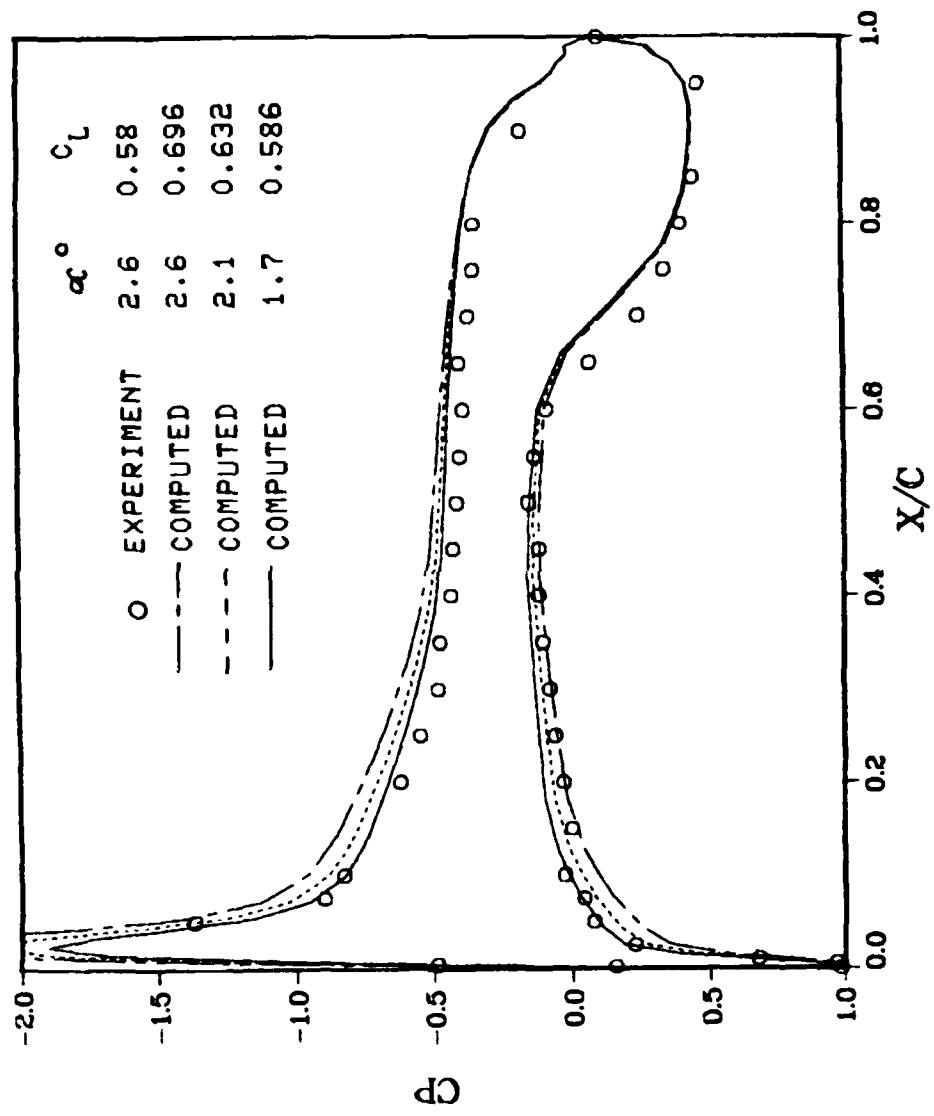


FIGURE 7 Variation of Computed C_p and C_l with Angle of Attack,
Subcritical Case

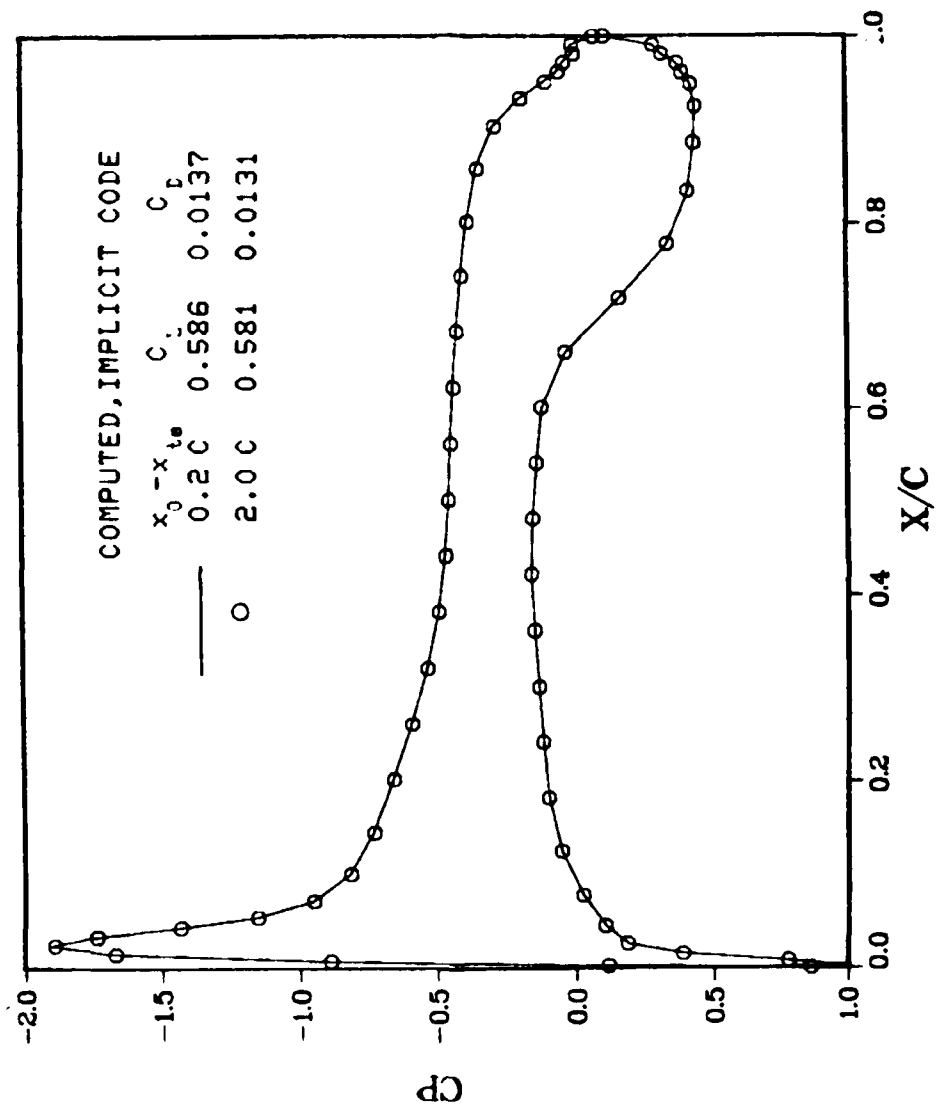
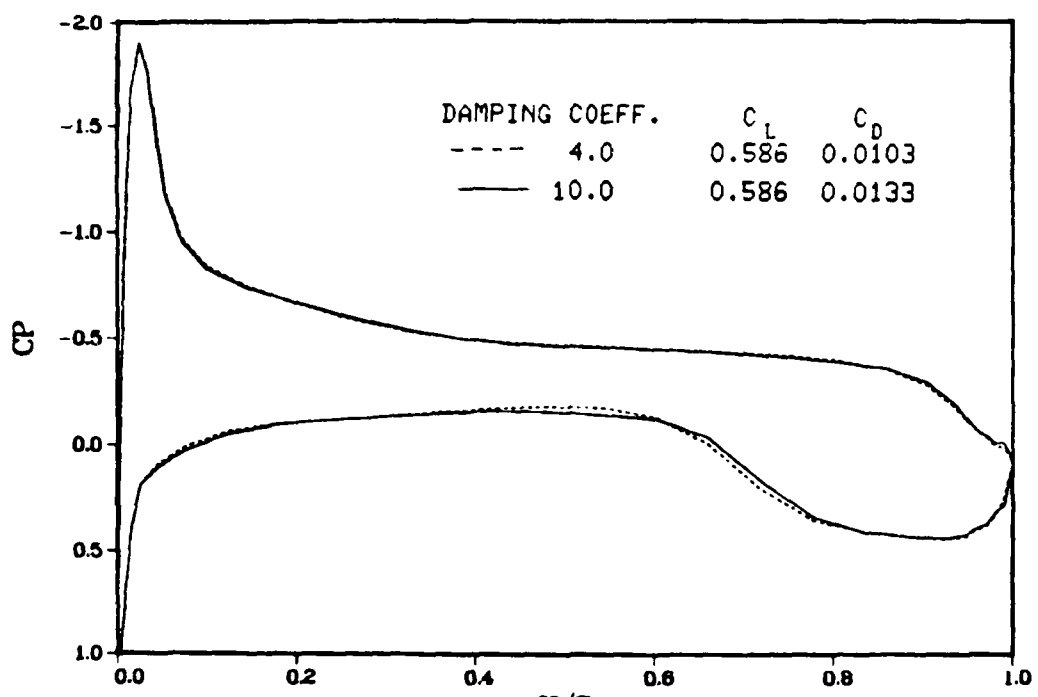
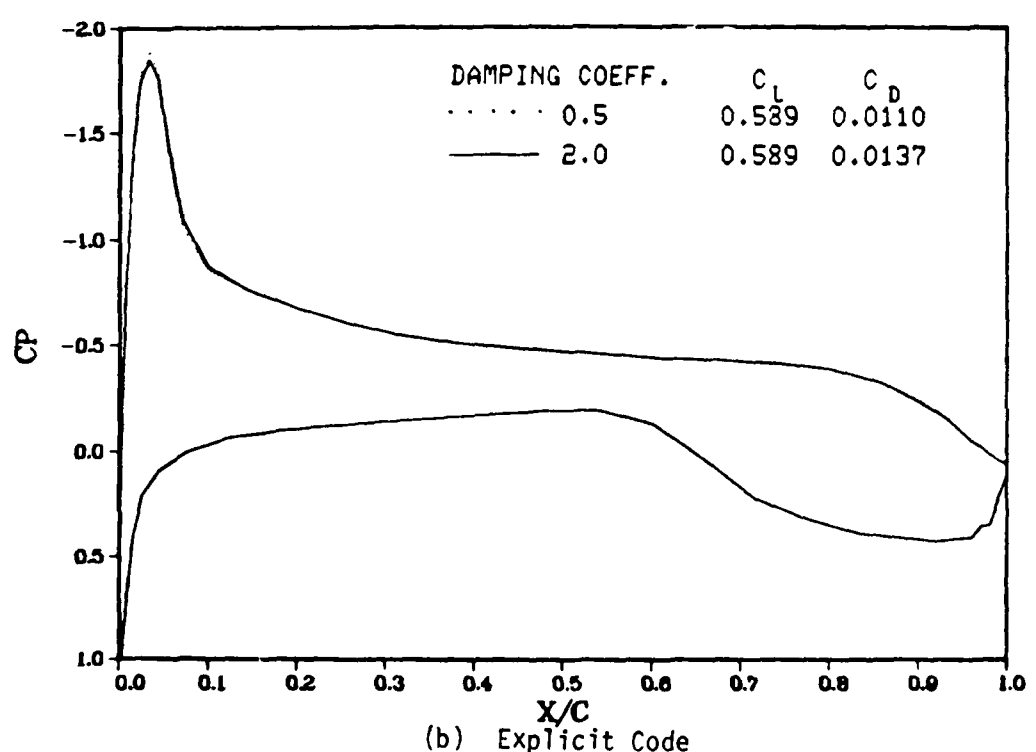


FIGURE 8 Effect of Variation of Near-Wake Relaxation Length (Equation (2.31)), Subcritical Case



(a) Implicit Code



(b) Explicit Code

FIGURE 9 Effect of Damping Coefficient on Subcritical Case, Coarse Grid

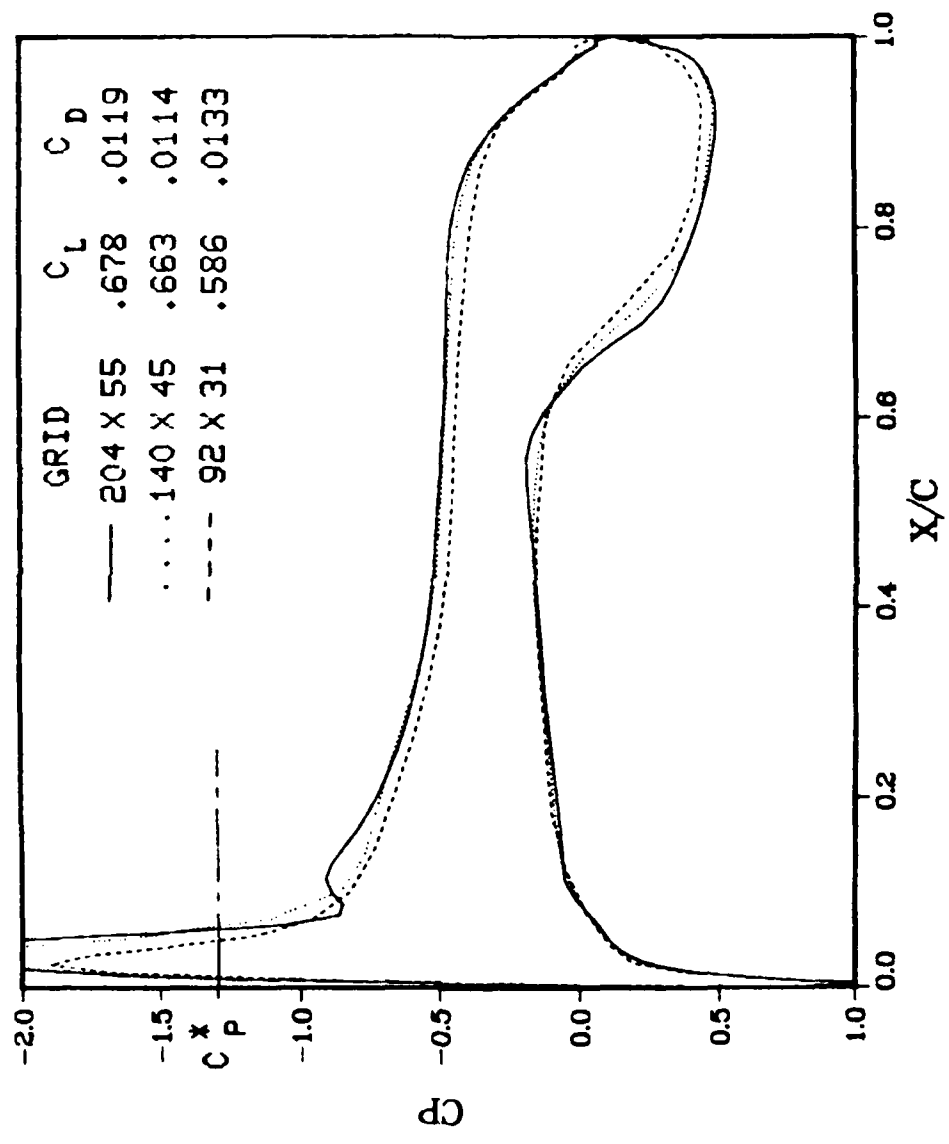
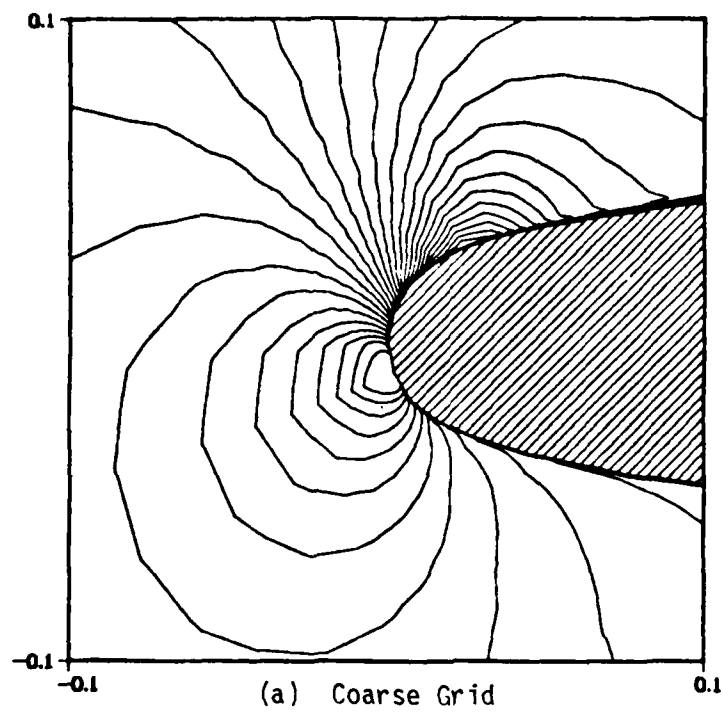
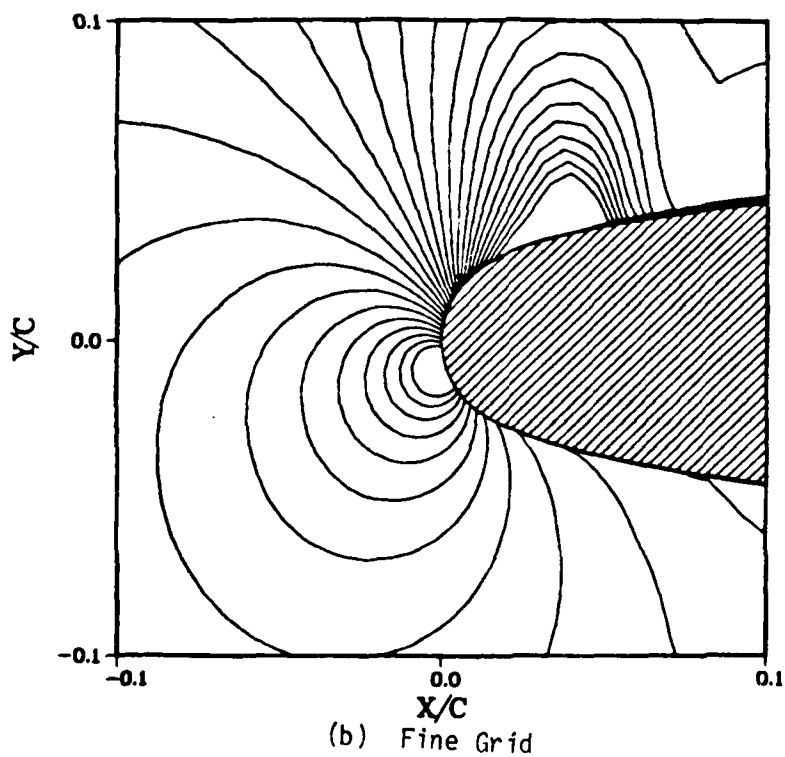


FIGURE 10 Effect of Grid Resolution on Computed Subcritical Flow, Implicit Code



(a) Coarse Grid



(b) Fine Grid

FIGURE 11 Computed Mach Number Contours for Subcritical Case, Implicit Code

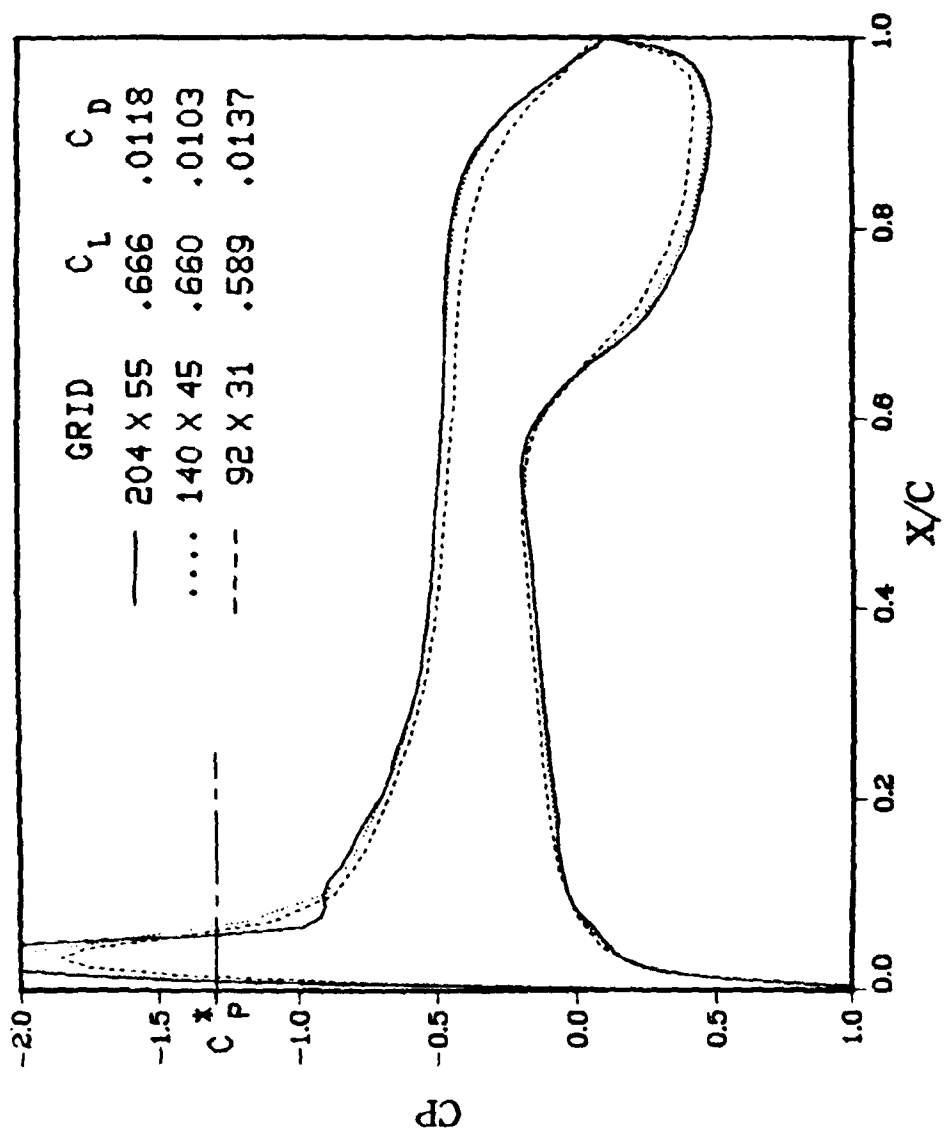
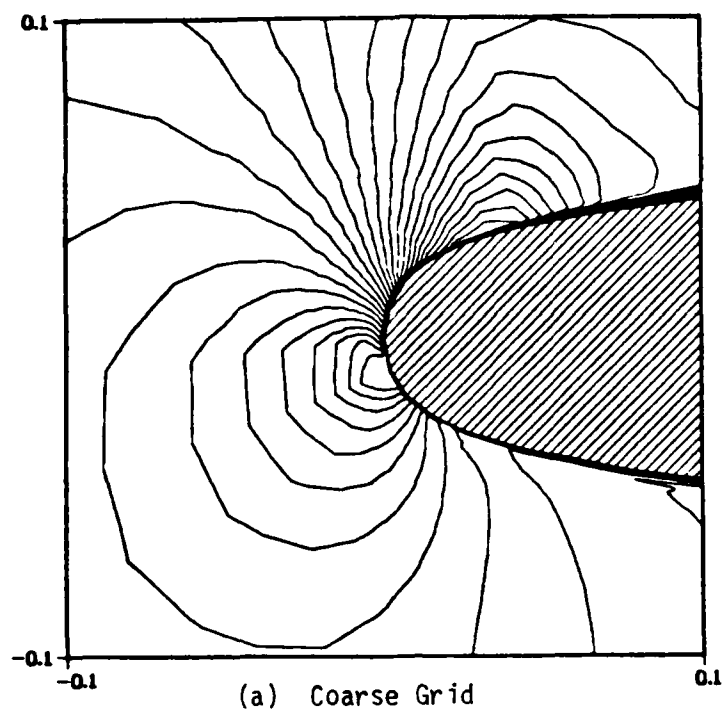
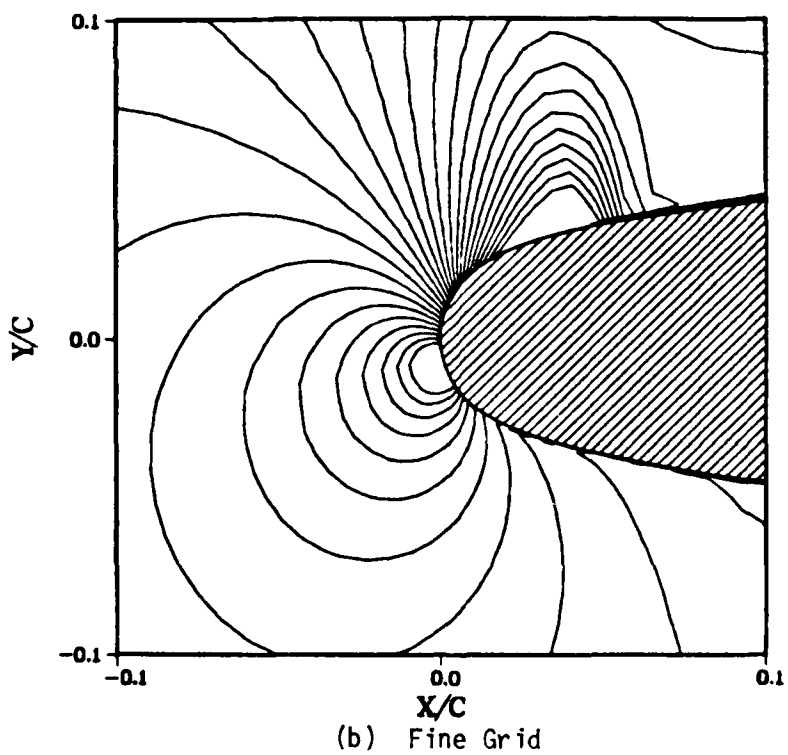


FIGURE 12 Effect of Grid Resolution on Computed Subcritical Flow, Explicit Code



(a) Coarse Grid



(b) Fine Grid

FIGURE 13 Computed Mach Number Contours for Subcritical Case, Explicit Code

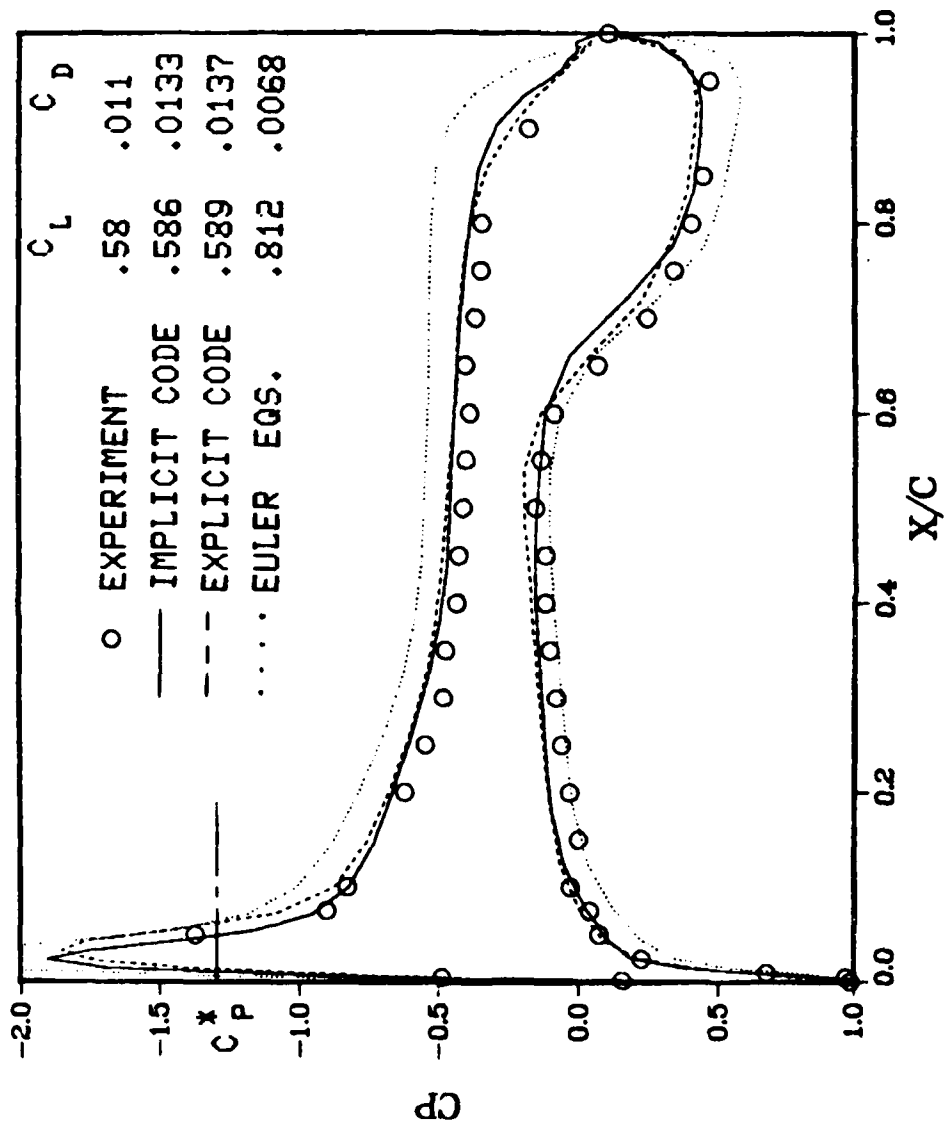


FIGURE 14 Computed and Experimental C_p , C_L and C_D for subcritical Case, Coarse Grid

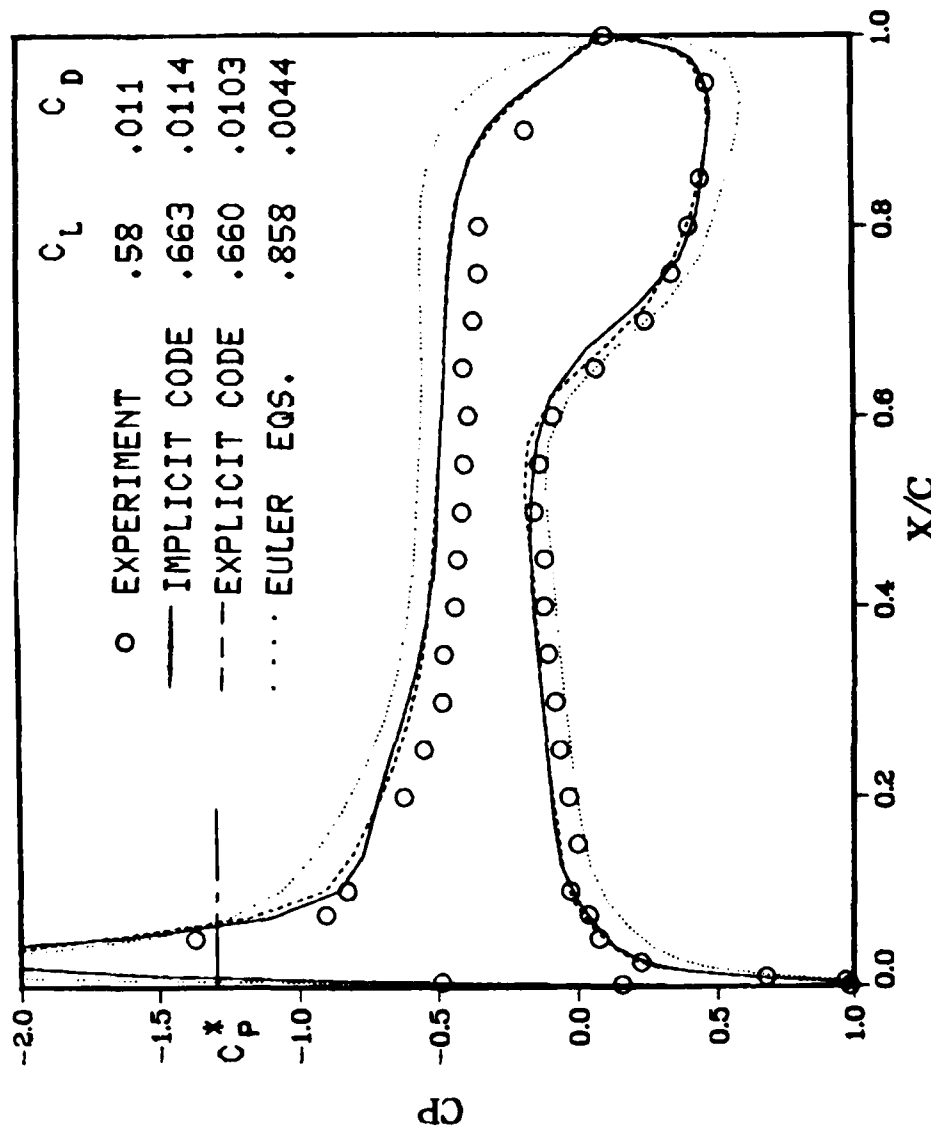


FIGURE 15 Computed and Experimental C_P , C_L and C_D for Subcritical Case, Medium Grid

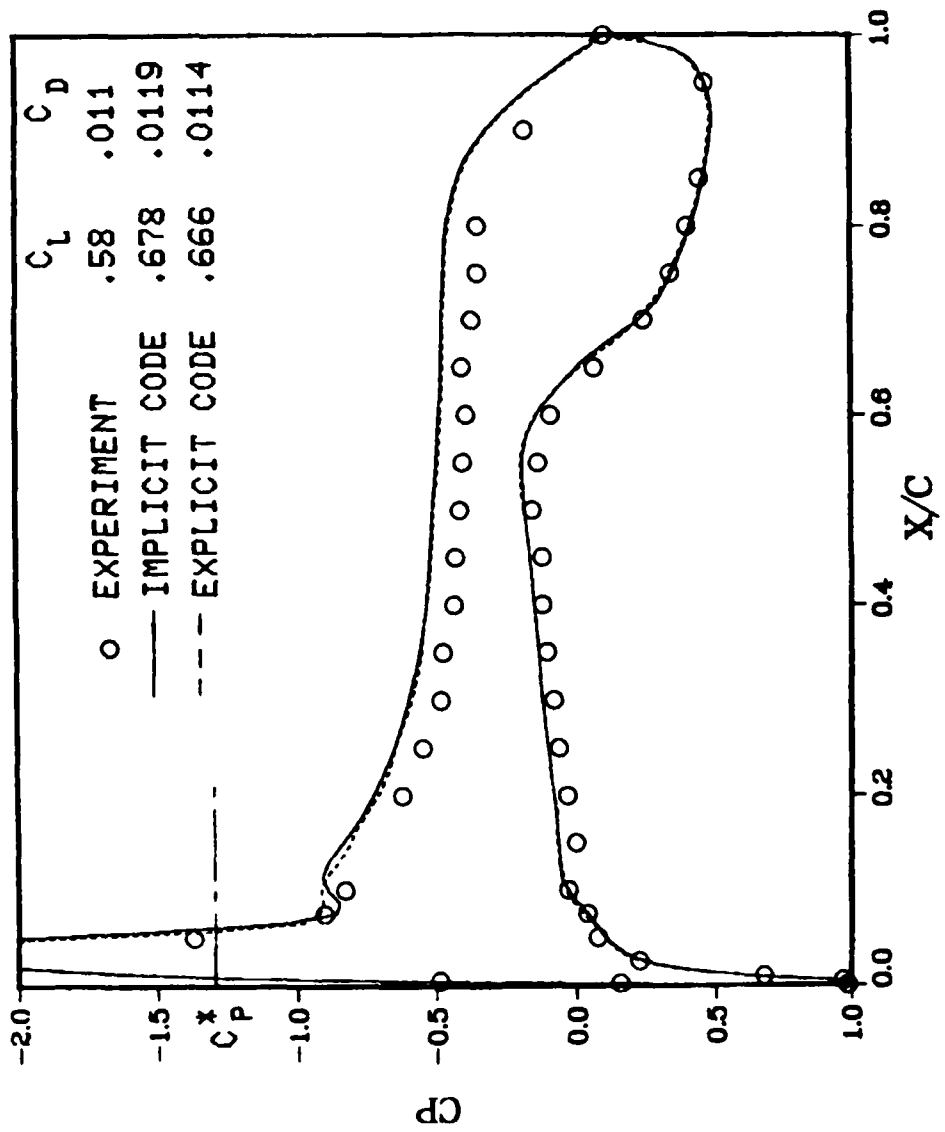


FIGURE 16 Computed and Experimental C_P , C_L and C_D for Subcritical Case, Fine Grid

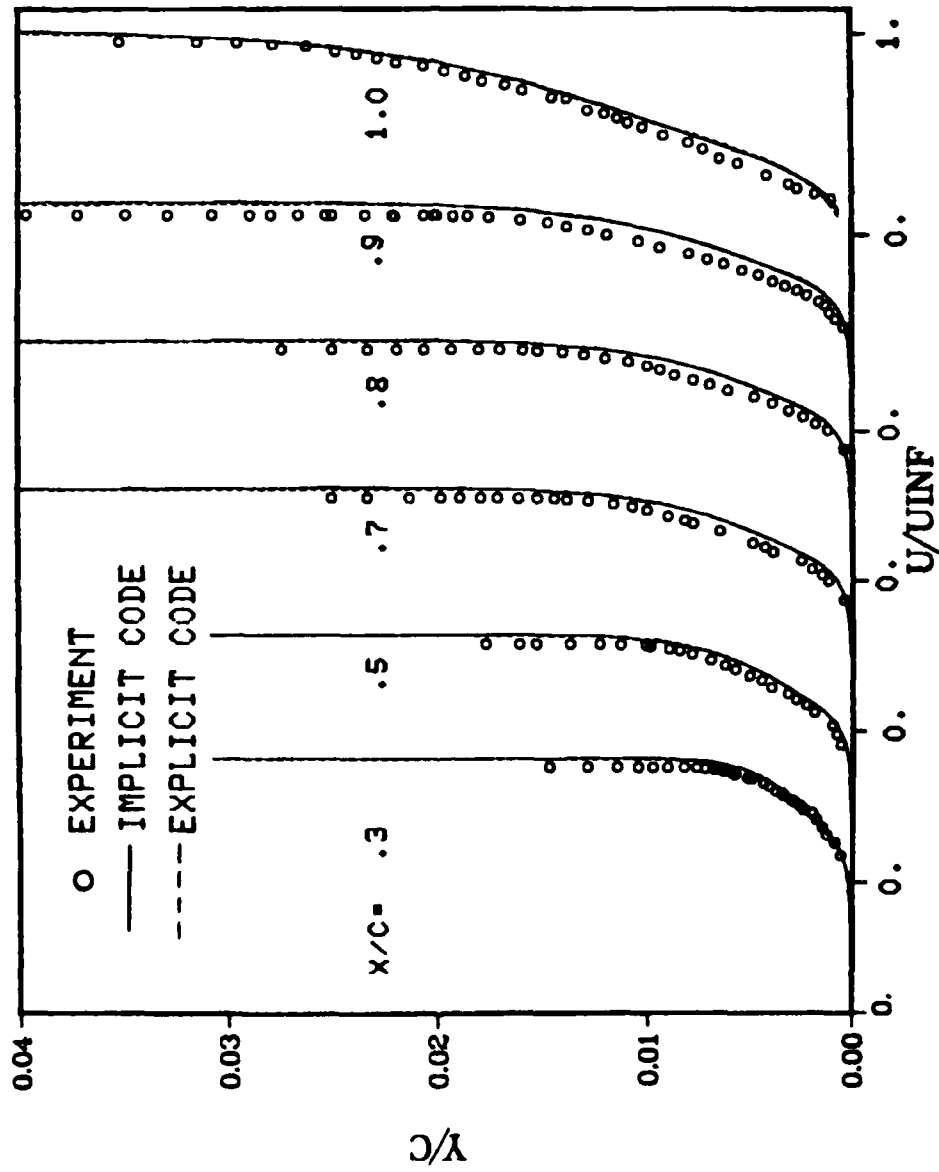


FIGURE 17 Computed and Experimental Velocity Profiles for Subcritical Case, Upper Surface

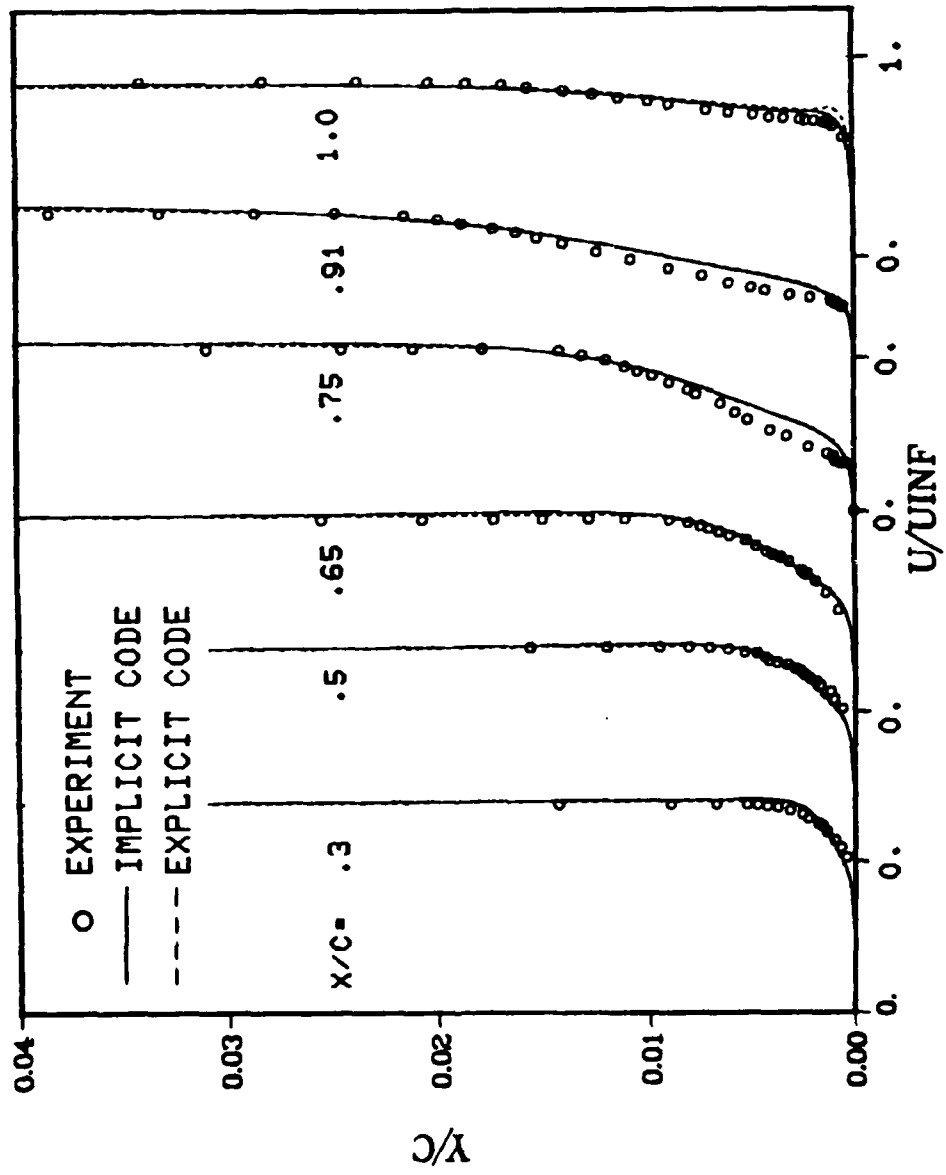


FIGURE 18 Computed and Experimental Velocity Profiles for Subcritical Case, Lower Surface

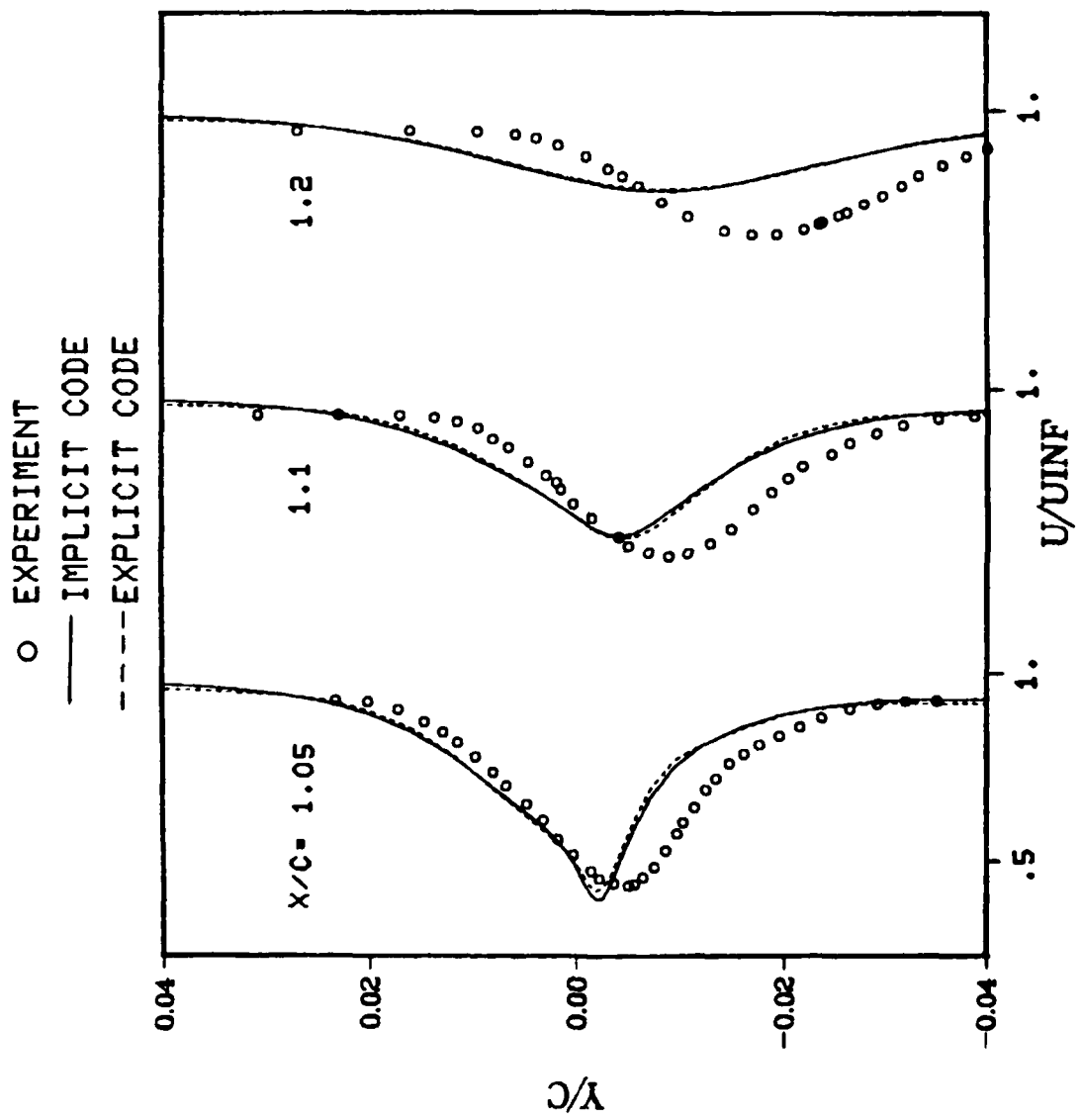
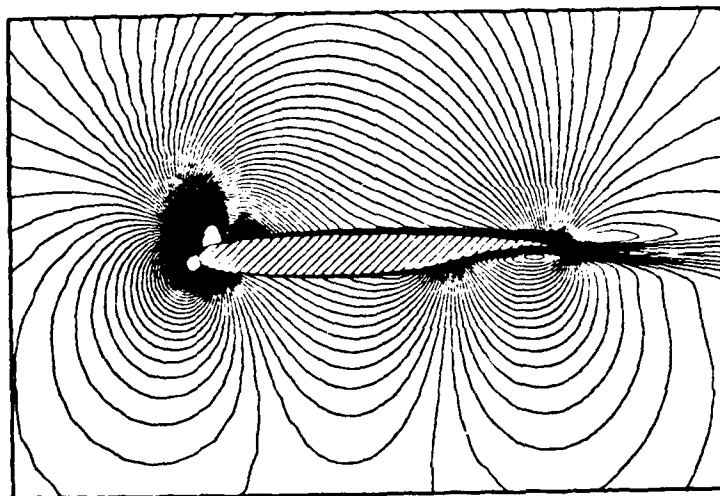
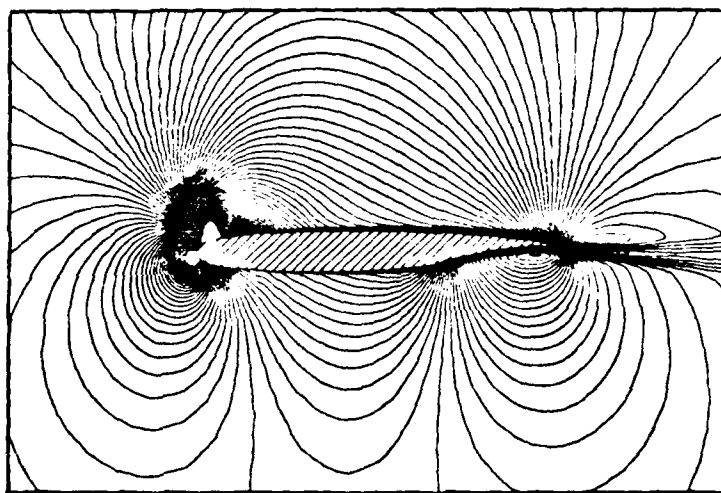


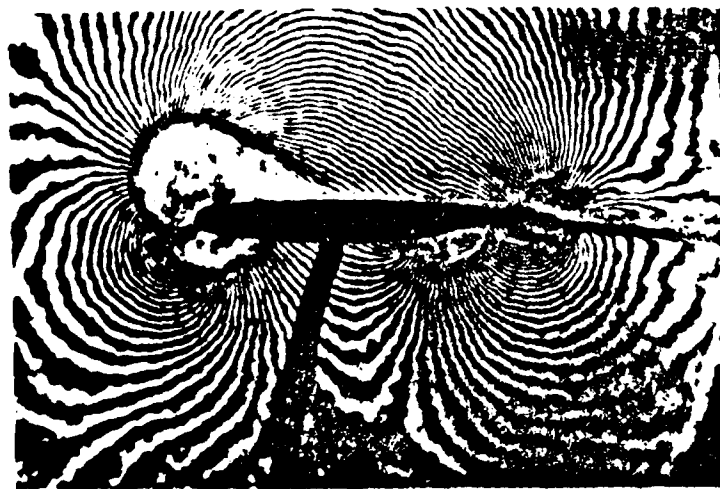
FIGURE 19 Computed and Experimental Velocity Profiles for Subcritical Case, Near-Wake



(a) Implicit Code

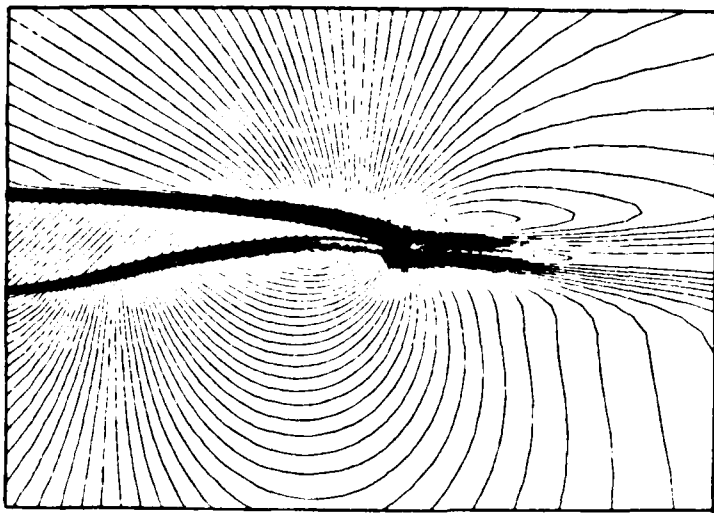


(b) Explicit Code

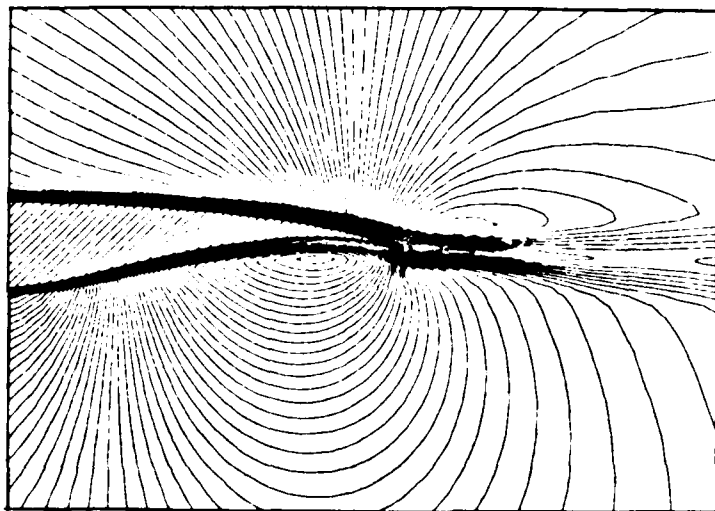


(c) Experiment

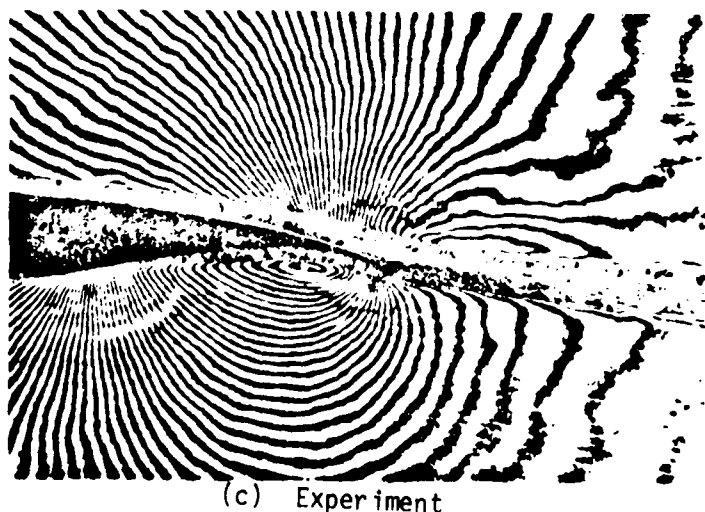
FIGURE 20 Comparison of Computed Density Contours and Experimental Interferogram, Subcritical Case



(a) Implicit Code

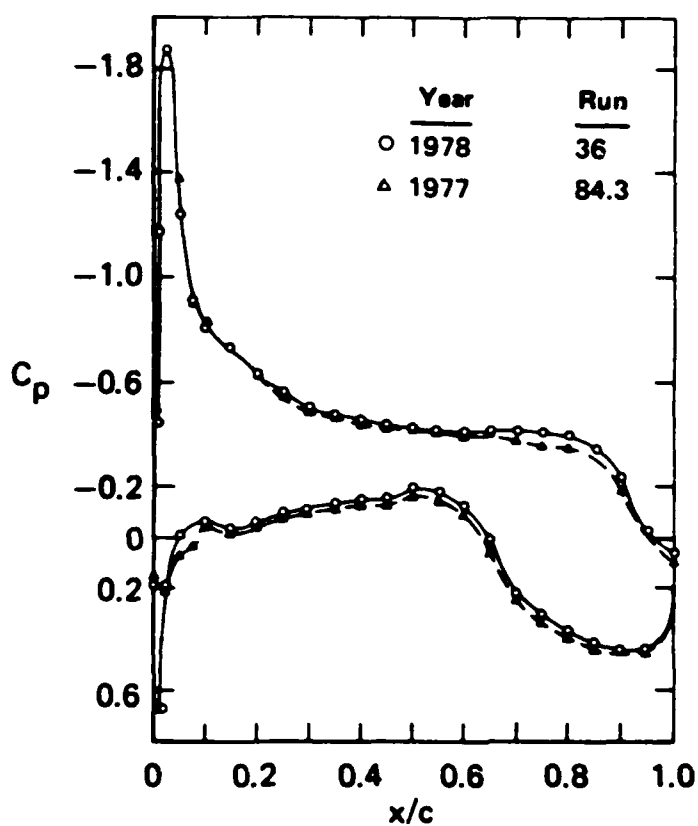


(b) Explicit Code

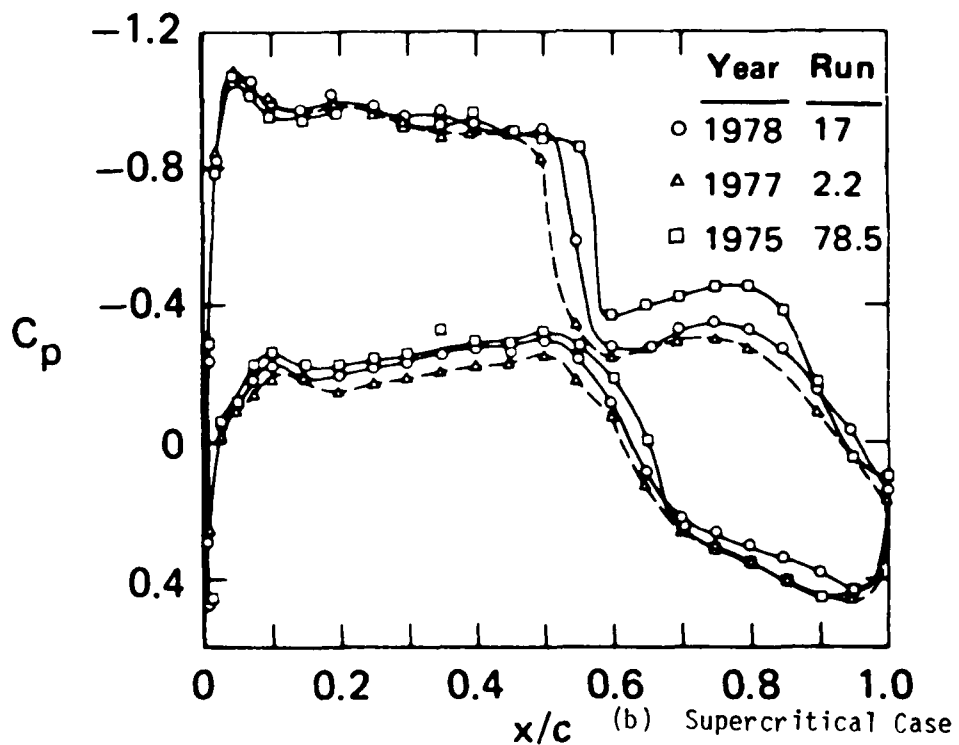


(c) Experiment

FIGURE 21 Detailed Comparison of Computed Density Contours and Experimental Interferogram near Airfoil Trailing Edge, Subcritical Case



(a) Subcritical Case



(b) Supercritical Case

FIGURE 22 Repeatability of Experimental Static-Pressure Measurements
(Reference 4)

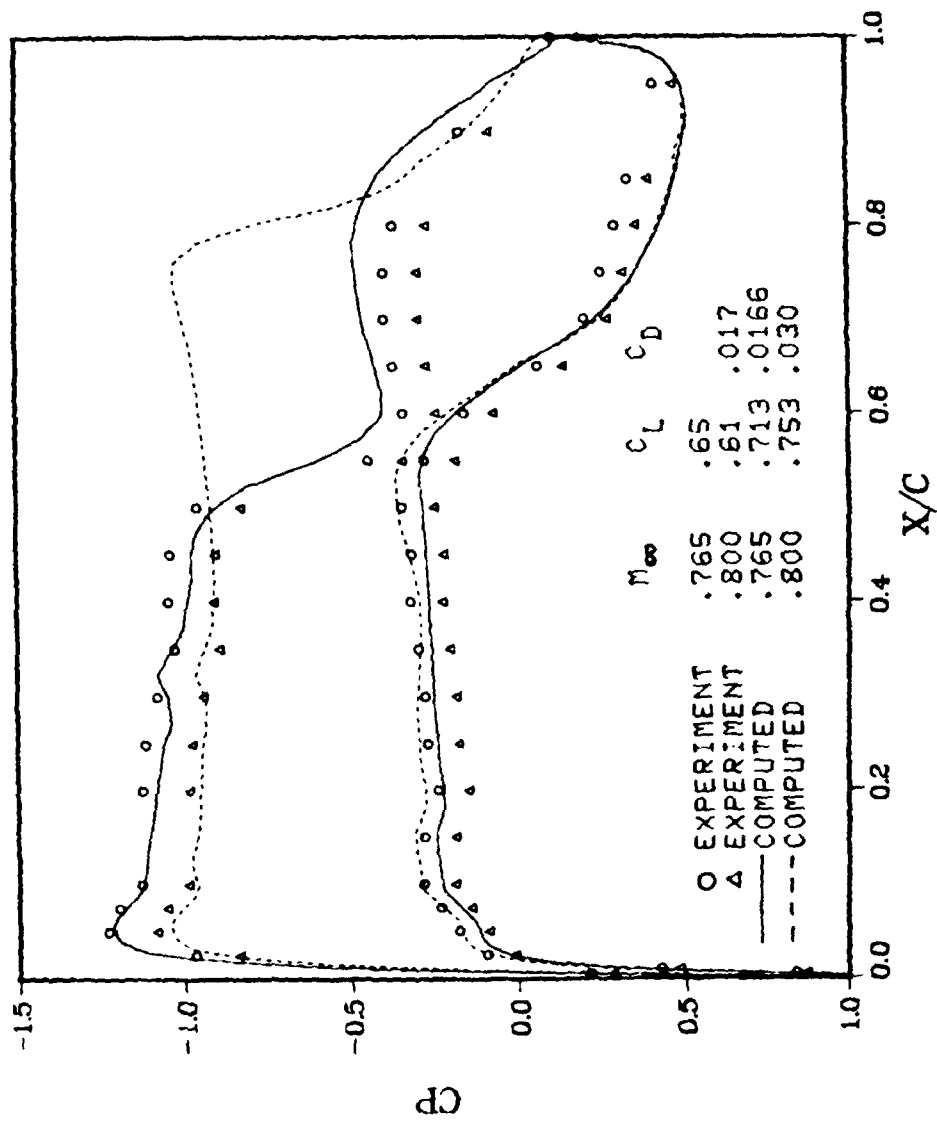


FIGURE 23 Effect of Freestream Mach Number on Shock Location for Supercritical Case, Explicit Code

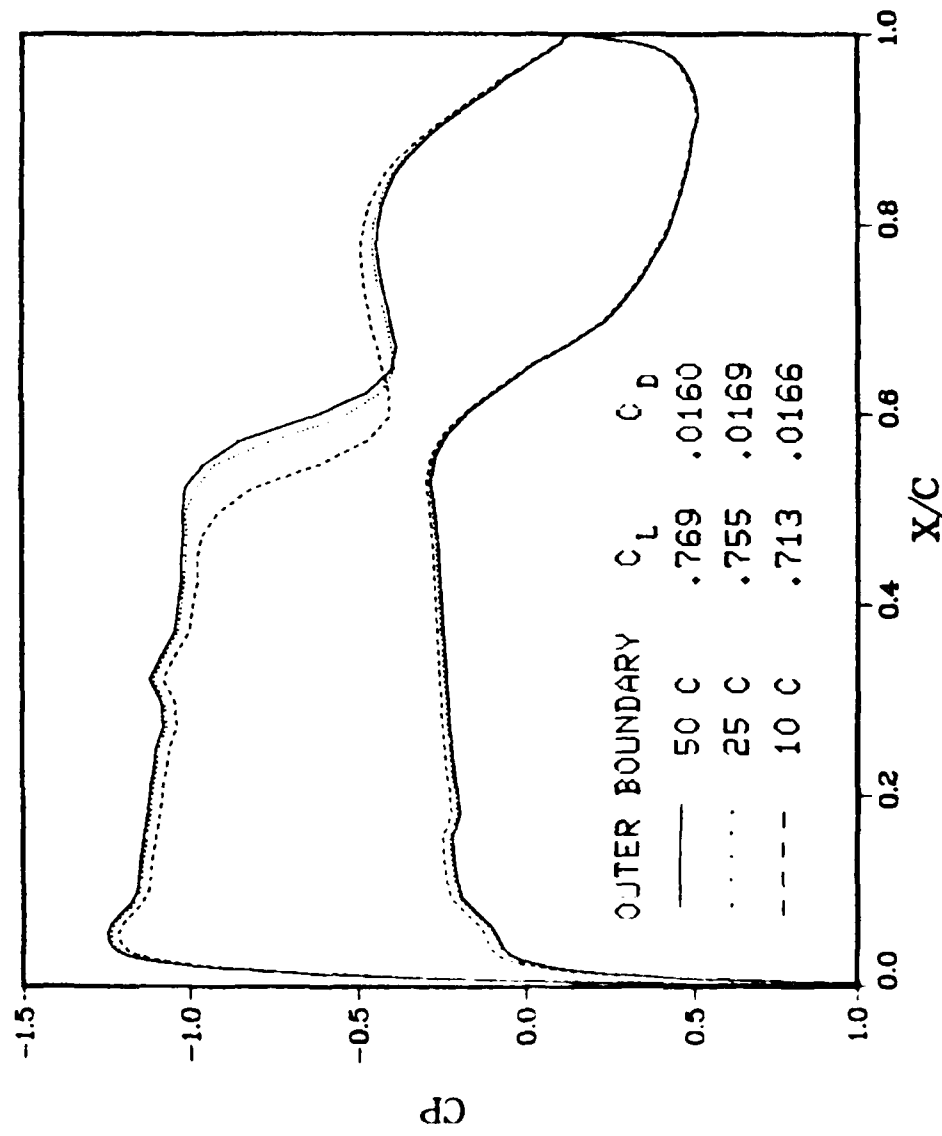


FIGURE 24 Effect of Fairfield Boundary Placement on Computed
Supercritical flow, Explicit Code

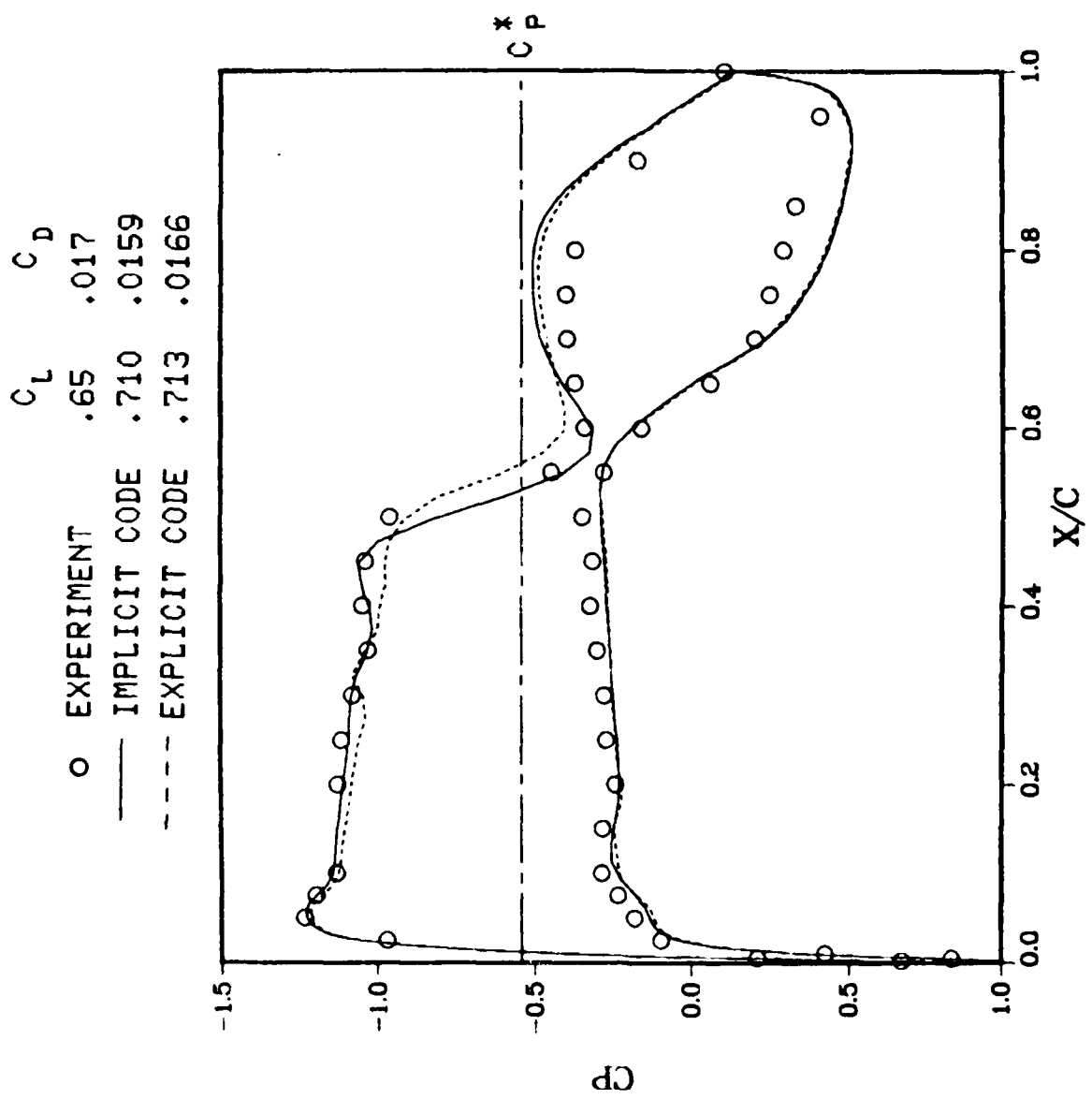


FIGURE 25 Computed and Experimental C_P , C_L and C_D for Supercritical Case

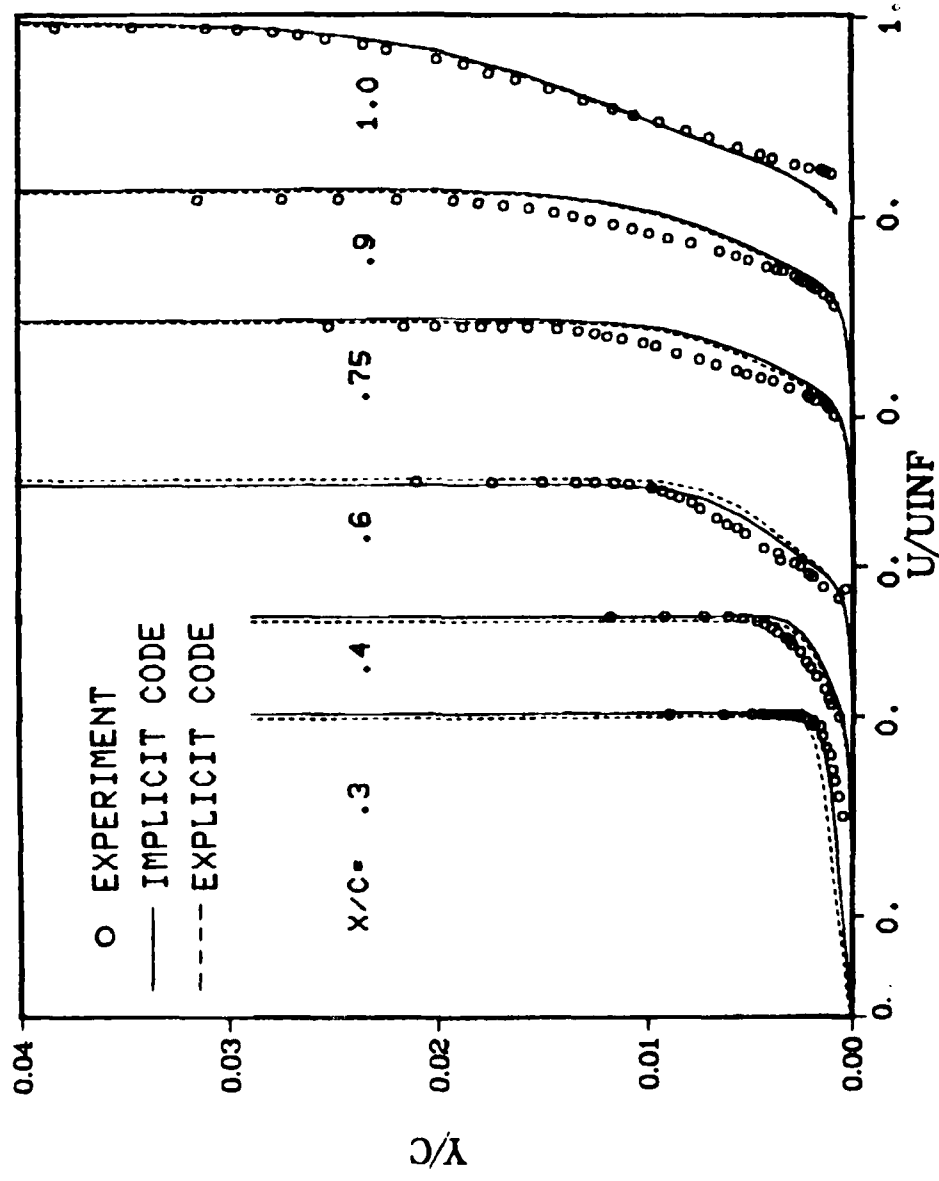


FIGURE 26 Computed and Experimental Velocity Profiles for Supercritical Case, Upper Surface

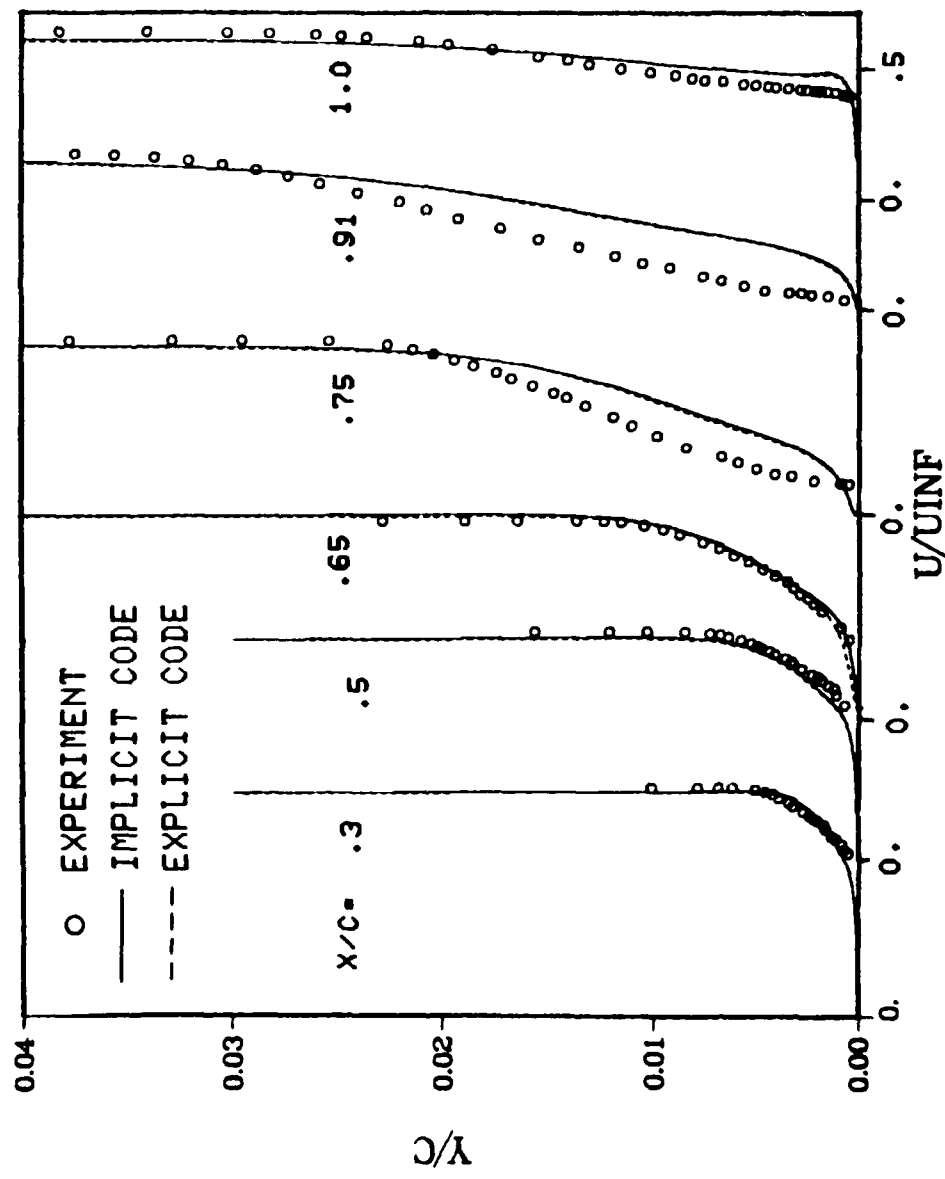


FIGURE 27 Computed and Experimental Velocity Profiles for Supercritical Case, Lower Surface

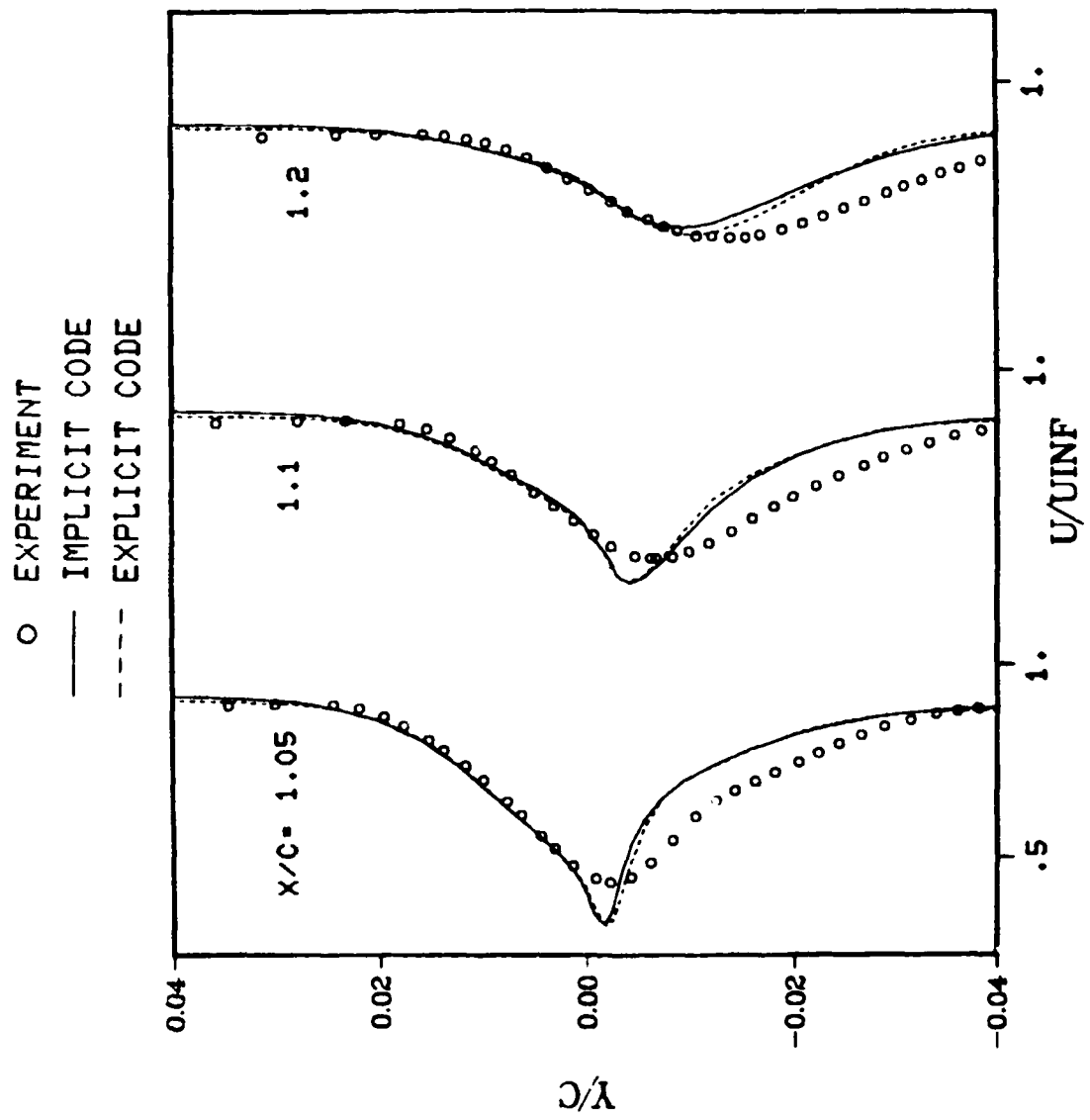
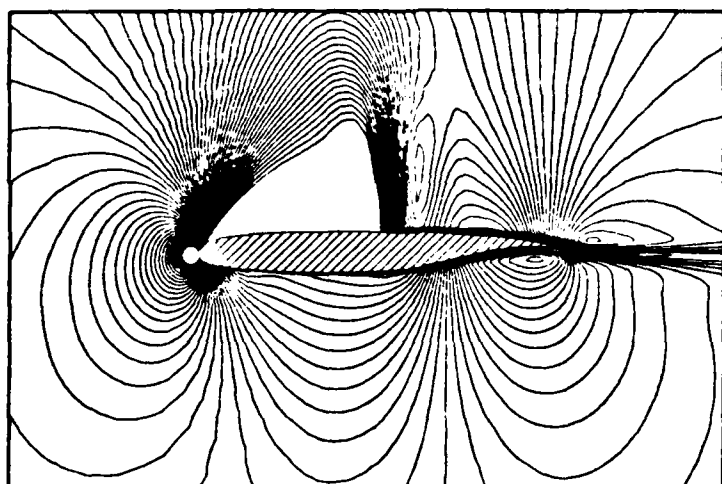
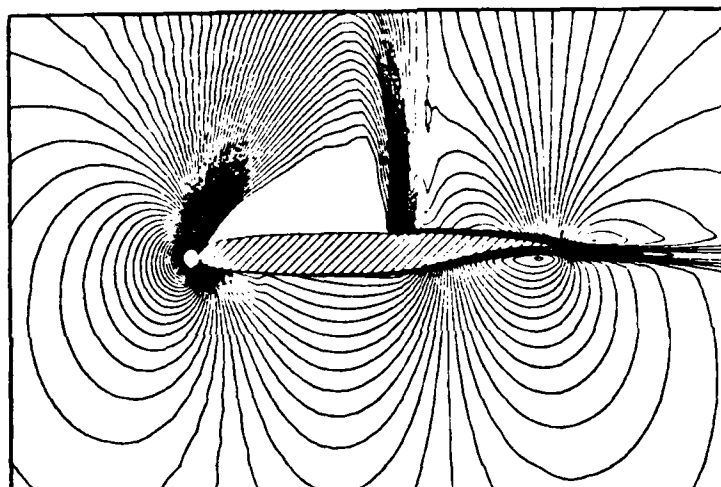


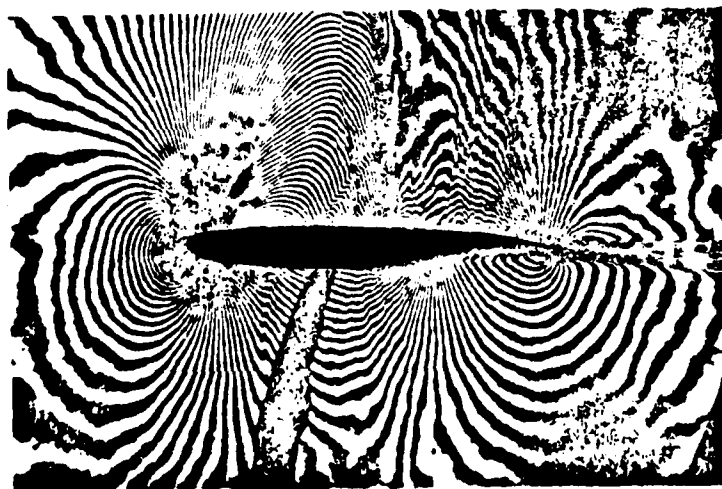
FIGURE 28 Computed and Experimental Velocity Profiles for Supercritical Case, Near-Make



(a) Implicit Code



(b) Explicit Code



(c) Experiment

FIGURE 29 Comparison of Computed Density Contours and Experimental Interferogram, Supercritical Case

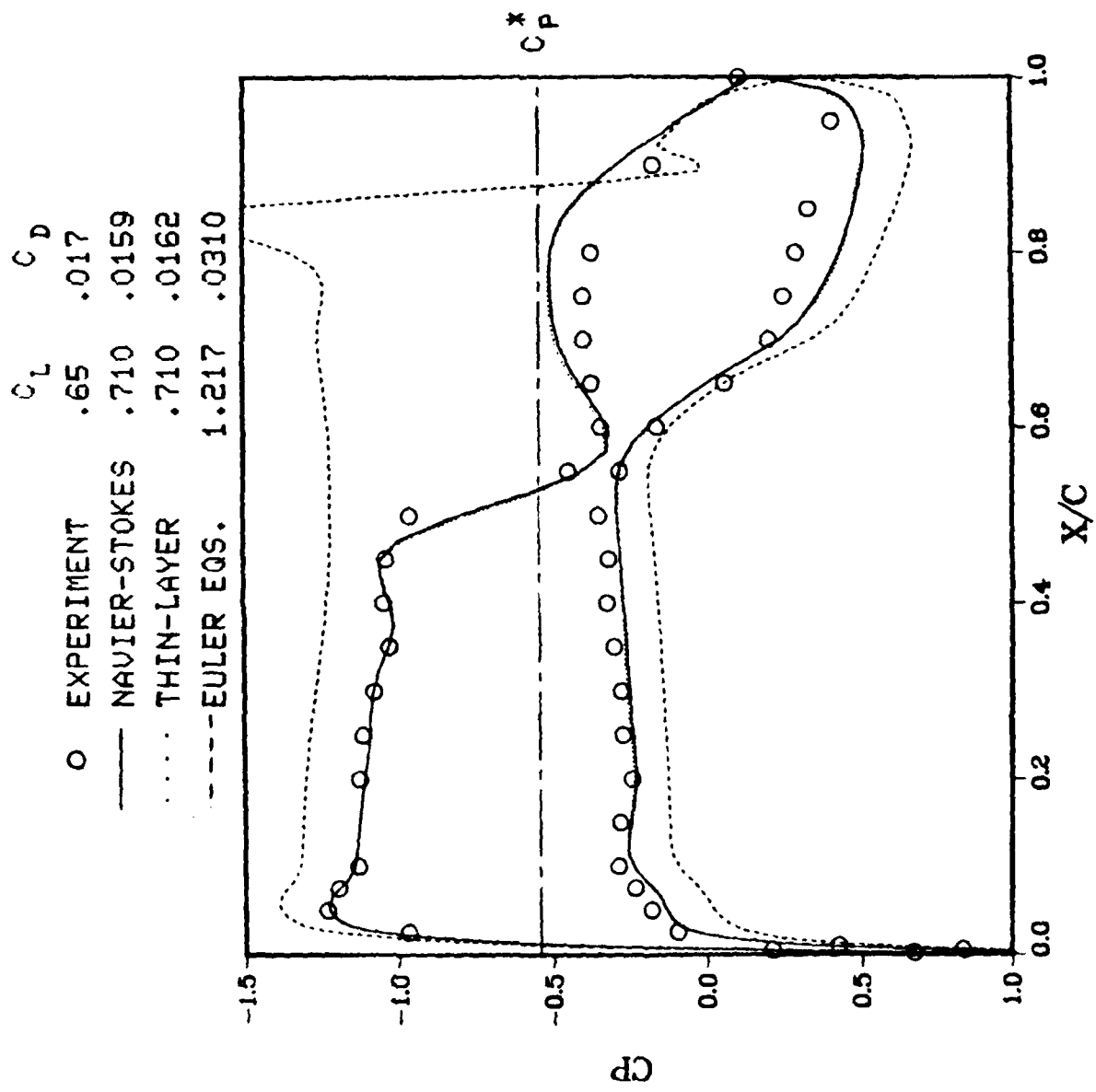


FIGURE 30 Comparison of Euler, Thin-Layer and Navier-Stokes Results for Supercritical Case, Implicit Code

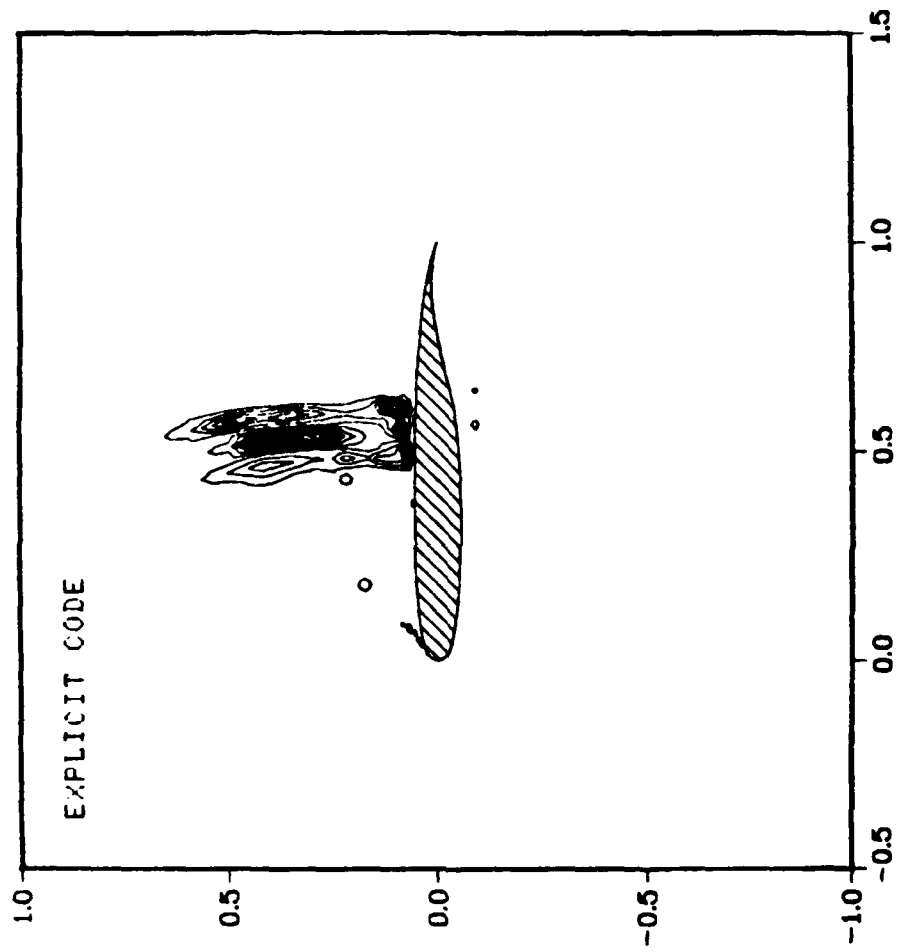
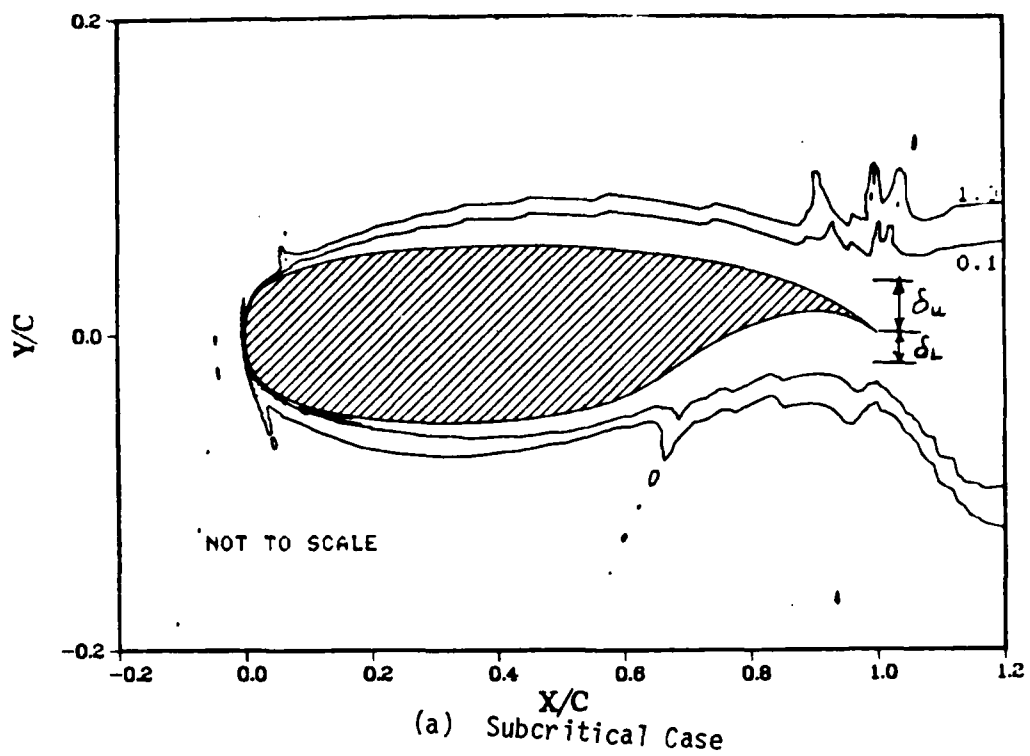
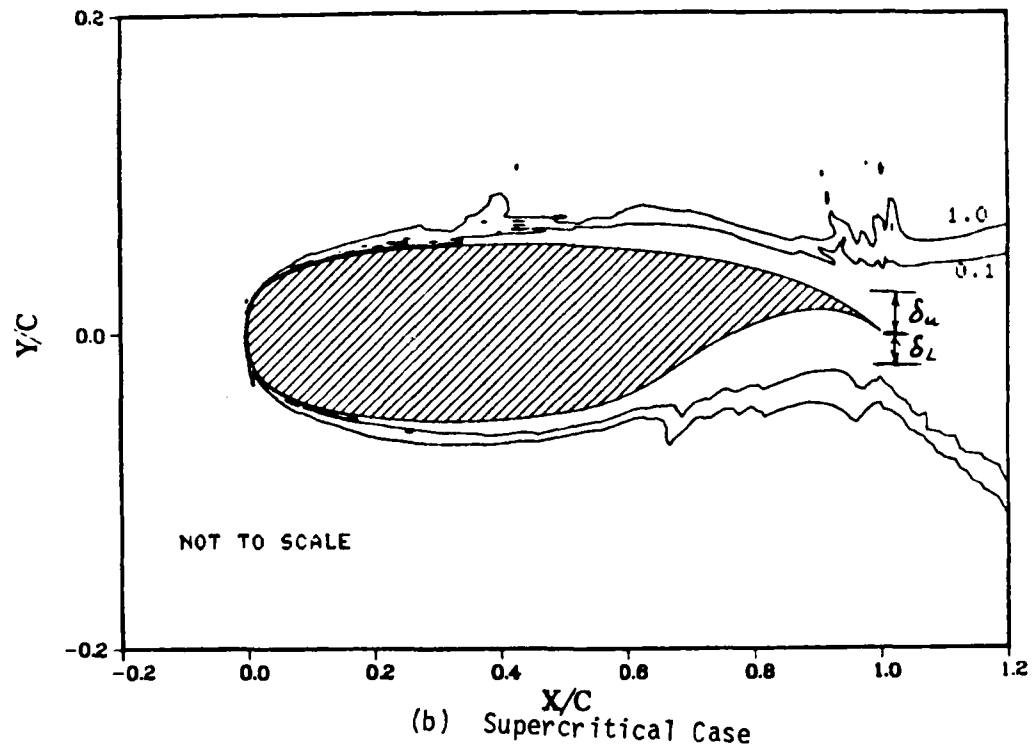


FIGURE 31 Contours of Damping-to-Truncation Error Ratio for
Density Equation, Supercritical Case



(a) Subcritical Case



(b) Supercritical Case

FIGURE 32 Contours of Artificial-to-True Viscosity Ratio in Streamwise Momentum Equation, Explicit Code (Fine Grid)

REFERENCES

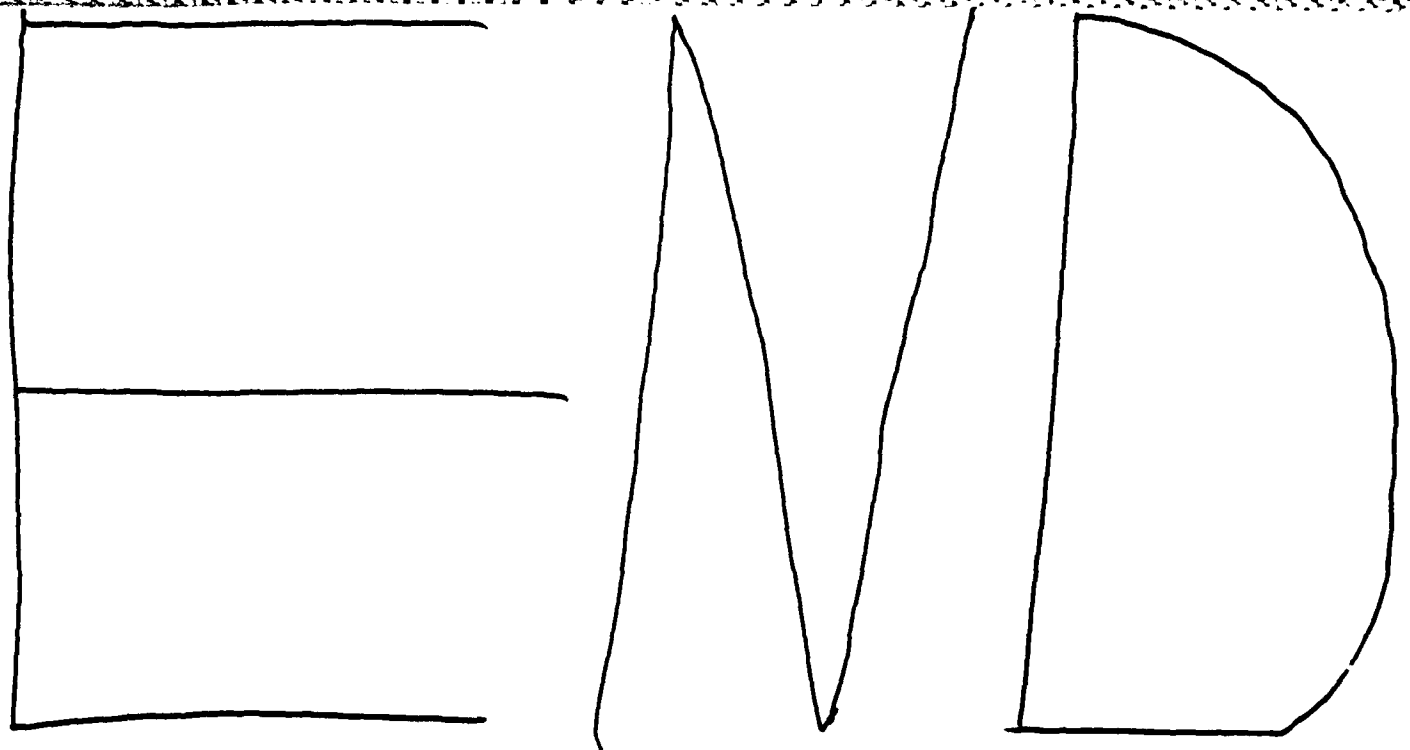
1. Mehta, U., and Lomax, H., "Reynolds Averaged Navier-Stokes Computations of Transonic Flows-the-State-of-the-Art," Transonic Aerodynamics, AIAA, New York, 1982.
2. Shang, J., "An Assessment of Numerical Solutions of the Compressible Navier-Stokes Equations," AIAA Paper 84-1549, 1984.
3. Pulliam, T., "Euler and Thin Layer Navier-Stokes Codes: ARC2D, ARC3D," Notes for Computational Fluid Dynamics User's Workshop, The University of Tennessee Space Institute, 1984.
4. Spaid, W., et al, "An Experimental Study of Transonic Flow about a Supercritical Airfoil," NASA TM-81336, 1983.
5. Kline, S., et al., Proceedings of 1980-1981 AFOSR-HTM-Stanford Conference on Complex Turbulent Flows, Vol. I, 1982.
6. Rubesin, M., and Rose, W., "The Turbulent Mean-Flow, Reynolds-Stress and Heat-Flux Equations in Mass Averaged Dependent Variables," NASA TMX-62248, 1973.
7. Baldwin, B., and Lomax, H., "Thin Layer Approximation and Algebraic Model for Separated Turbulent Flows," AIAA Paper 78-257, 1978.
8. Visbal, M., and Knight, D., "Generation of Orthogonal and Nearly Orthogonal Coordinates with Grid Control Near Boundaries," AIAA J., Vol. 20, No. 3, 1982.
9. MacCormack, R.W., "The Effect of Viscosity in Hypervelocity Impact Cratering," AIAA Paper 69-354, 1969.
10. Beam, R., and Warming, R., "An Implicit Factored Scheme for the Compressible Navier-Stokes Equations," AIAA J., Vol. 16, 1978.
11. Shang, J., and Hankey, W., "Numerical Solution of the Navier-Stokes Equations for a Three-Dimensional Corner," AIAA J., Vol. 15, No. 11, 1977.
12. Pulliam, T., and Steger, J., "Implicit Finite Difference Simulation of Three-Dimensional Compressible Flow," AIAA J., Vol. 18, No. 2, 1980.
13. Schlichting, H., Boundary Layer Theory, 6th Edition, MacGraw-Hill, New York, 1968.
14. Hegna, H., "The Numerical Solution of the Navier-Stokes Equations for Incompressible Turbulent Flow over Airfoils," AFWAL-TR-81-3053, 1981.

REFERENCES (Continued)

15. Bradshaw, P., et al, "Calculation of Interacting Turbulent Shear Layers: Duct Flow," Trans. ASME Series I: J. Fluids Eng., 95, 1973.
16. Visbal, M., "Generation of Nearly-Orthogonal Body-Fitted Coordinate System in Two-Dimensional Singly-Connected Regions," M.S. Thesis, Rutgers University, New Jersey, 1980.
17. Visbal, M., and Knight, D., "Generation of Orthogonal and Nearly-Orthogonal Boundary-Fitted Coordinates with Direct Control of Grid Spacing," Report RU-TR-154-MIAE-F, Dept. of Mechanical and Aerospace Engineering, Rutgers University, New Jersey, 1981.
18. Thompson, J., et al, "Automatic Numerical Generation of Body-Fitted Curvilinear Coordinate System for Field Containing any Number of Arbitrary Two-Dimensional Bodies," J. Comp. Phys., Vol. 15, 1974.
19. Desideri, J., et al, "On Improving the Iterative Convergence Properties of an Implicit Approximate-Factorization Finite Difference Algorithm," NASA TM-78495, 1978.
20. Srinivasan, G., et al, "Computation of Simple 3-D Wing-Vortex Interaction in Transonic Flow," AIAA Paper 81-1206, 1981.
21. Visbal, M., and Knight, D., "The Baldwin-Lomax Turbulence Model for Two-Dimensional Shock-Wave/Boundary-Layer Interactions," AIAA J., Vol. 22, No. 7, 1984.
22. MacCormack, R., "Numerical Solution of the Interaction of a Shock Wave with a Laminar Boundary Layer," Lecture Notes in Physics, Vol. 8, 1971.
23. Shang, J., et al, "Performance of a Vectorized Three-Dimensional Navier-Stokes Code on a Cray-1 Computer," AIAA J., Vol. 18, No. 9, 1980.
24. Steger, J., "Coefficient Matrices for Implicit Finite Difference Solution of the Inviscid Fluid Conservation Law Equations," Computer Methods in Applied Mechanics and Engineering, Vol. 13, 1978.
25. Pulliam, T., and Chaussee, D., "A Diagonal Form of an Implicit Approximate Factorization Algorithm," J. Comp. Phys., Vol. 39, 1981.
26. Steger, J., "Implicit Finite-Difference Simulation of Flow About Arbitrary Two-Dimensional Geometries," AIAA J., Vol. 16, No. 7, 1978.

REFERENCES (Continued)

27. Chyu, W., and Kuwahara, K., "Computations of Transonic Flow Over an Oscillating Airfoil with Shock-Induced Separation," AIAA Paper 82-0350, 1982.
28. Degani, D., and Steger, J., "Comparison Between Navier-Stokes and Thin-Layer Computations for Separated Supersonic Flow," AIAA J., Vol. 21, No. 11, 1983.



12-86

